10.13147/SOE.2017.009

Ph.D. Dissertation
University of Sopron (Soproni Egyetem)
The Simonyi Károly Faculty of Engineering,
Wood Sciences and Applied Arts
The Cziráki József Doctoral School of Wood Sciences and Technologies

ATR-FTIR Study of the Interaction of CO_2 with Bacterial cellulose-Based Membranes

Author: YANIN HOSAKUN
Research Supervisor: Prof. Dr. LEVENTE CSÓKA

Sopron

2017

10.13147/SOE.2017.009

ATR-FTIR Study of the Interaction of CO_2 with Bacterial cellulose-Based Membranes

Értekezés doktori (PhD) fokozat elnyerése érdekében

a Soproni Egyetem Cziráki József Faanyagtudomány és Technológiák Doktori Iskolája Rosttechnikai és nanotechnológiai tudományok programja

Írta:
YANIN HOSAKUN

Készült a Soproni Egyetem Cziráki József Faanyagtudomány és Technológiák Doktori Iskola Rosttechnikai és nanotechnológiai tudományok programja keretében

Témavezető: Prof. Dr. Csóka Levente

Elfogadásra javaslom (igen / nem)

(aláírás)

A jelölt a doktori szigorlaton …........ % -ot ért el,

Sopron, 2016.11.29.

……………………...............

a Szigorlati Bizottság elnöke

Az értekezést bírálóként elfogadásra javaslom (igen /nem)

Első bíráló (Dr. …...................... …................) igen /nem

(aláírás)

Második bíráló (Dr. …...................... …................) igen /nem

(aláírás)

(Esetleg harmadik bíráló (Dr. …...................... …................) igen /nem

(aláírás)

A jelölt az értekezés nyilvános vitáján…..........% - ot ért el

Sopron,

………………………..
a Bírálóbizottság elnöke

A doktori (PhD) oklevél minősítése…...............................

………………………..
Az EDHT elnöke

10.13147/SOE.2017.009

I, the undersigned *Yanin Hosakun*, hereby declare that the Ph.D. dissertation, entitled "**ATR-FTIR Study of the Interaction of CO_2 with Bacterial cellulose-Based Membranes**", was carried out by myself for the degree of Doctor of Philosophy under supervision of Dr. Levente Csóka, Institute of Wood Based Products and Technologies, University of Sopron. The whole work is the result of my own investigation except where duly cited. The sources of information have been used and acknowledged in the content as well as the reference section.

Sopron, March 17th, 2017

……………………………………………..

Yanin Hosakun

10.13147/SOE.2017.009

Abstract

Bacterial cellulose (BC) was used as an active material for fabrication of the membrane for CO_2 adsorption study. The BC-membranes were further modified with silk fibroin protein and ZnO nanoparticles in order to increase the number of sites that may bind CO_2. The morphologies of all BC-based membranes were characterized by FESEM microscopy indicating that they were formed into a fine crisscross mesh structure with entangled nanofibrils. The interaction of the CO_2 with the membranes was investigated by means of ATR-FTIR spectroscopy. Heated membranes above 100°C, in order to remove some trapped CO_2 from atmosphere, were used as the control samples. After pressurizing the membranes in CO_2 at 3 bar for 8h, 16h, and 24h, FTIR spectra were recorded and compared to the spectra of the controls. The interaction of the membrane materials with CO_2 were studied by examining two regions of the spectra: 740-610 cm^{-1} (bending vibrations of CO_2) and 2400-2300 cm^{-1} (asymmetric stretching vibrations of CO_2). The envelopes of the bending and asymmetric stretching modes were deconvoluted into particular peaks by PeakFit software. The increase of the CO_2 absorbance in bending and asymmetric stretching features after CO_2 adsorption, together with the appearance of extra bands, is an evidence of CO_2 sorption to the membranes. Therefore, infrared studies showed that there was a strong interaction of CO_2 with BC-based membrane suggested by the Lewis acid-base type of interaction. The modified BC membranes spectra display broader and more splitting lines in both bending and asymmetric stretching modes signifying the introduction of silk fibroin and ZnO nanoparticles could increase the number of active sites for interaction with CO_2 to form more complex species. Additionally, it have been found that the specific sites in the modified BC membranes could facilitate the interaction with CO_2. These modified BC membranes could interact with CO_2 rapidly by demonstrating the optimum ability since 8h duration. On the other hand, the basic BC membrane was able to achieve the highest ability and be saturated by CO_2 after adsorption for 16h.

Table of Contents

Chapter **Page**

List of Figures

Figure **Page**

List of Tables

Table **Page**

10.13147/SOE.2017.009

CHAPTER I
INTRODUCTION AND PROBLEM STATEMENT

1.1 The CO_2 Problems

1.1.1 Greenhouse Gases and Global Warming

Greenhouse effect is a natural process which atmospheric gases absorb infrared radiation resulting in trapping of heat. Gases that absorb energy, on the other hand, slowing the rate at which the energy escapes to space are called *Greenhouse gases*. These gases act like a blanket insulating the Earth. The Greenhouse effect plays an important role in shaping the earth's climate. However, the changes in climate are not only owing to natural processes, human activities, such as burning fossil fuels, industrialization, and deforestation, also contribute to enhance the greenhouse effect. This enhanced greenhouse effect results from an increase in the concentrations of the greenhouse gases which influences on the increasing in global mean temperature ("The Greenhouse Effect and Climate Change", 2014; "Overview of Greenhouse Gases", 2016; "Understanding Global Warming Potentials", 2016).

Greenhouse gases comprise of carbon dioxide (CO_2), water vapor (H_2O), methane (CH_4), nitrous oxide (N_2O), ozone (O_3), chlorofluorocarbons (CFCs), etc. It is interesting to note that the majority of emissions are CO_2. Since 1927 to 2006, the CO_2 emissions released from industry and combustion of fossil fuels have increased from 1 billion tons per year to 8 billion tons per year. CO_2 is a significant contributor to the global warming. It is emitted by human activities, natural processes; respiration and volcanic eruptions, and a by-product of the combustion of fossil fuels ("The top Ten Green House Gases", 2009; "The Greenhouse Effect and Climate Change", 2014; "A blanket around the Earth", 2016). The CO_2 emission is mainly come from electricity generation, transportation, industrial and residential use. The concentration of CO_2 has increased by 40% after the industrial revolution. The atmospheric CO_2 levels in recent years are illustrated in Figure 1. CO_2 is the fourth most abundant gas in atmosphere and is uniformly distributed over the Earth's surface with a concentration of about 404 ppm as shown in the graph. Its concentration has been rising annually (Galhotra and Grassian, 2010; Sun et al., "Coal Conversion and utilization for reducing CO_2 emissions from a power plant"; "Carbon Dioxide", 2016).

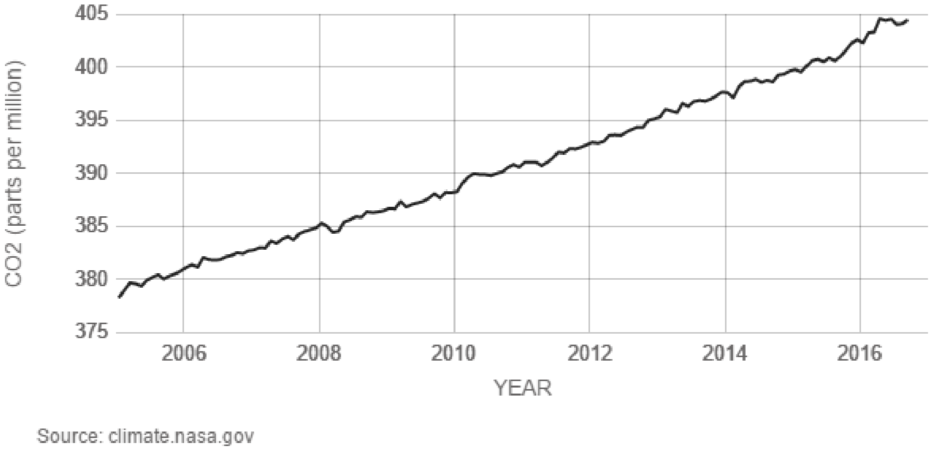

Source: climate.nasa.gov

Figure 1. CO_2 levels in atmosphere (“Carbon Dioxide”, 2016).

The change in global surface temperature relative to 1951-1980 average temperatures is demonstrated in Figure 2. As can be seen, in 2015, it ranks as the warmest on record.

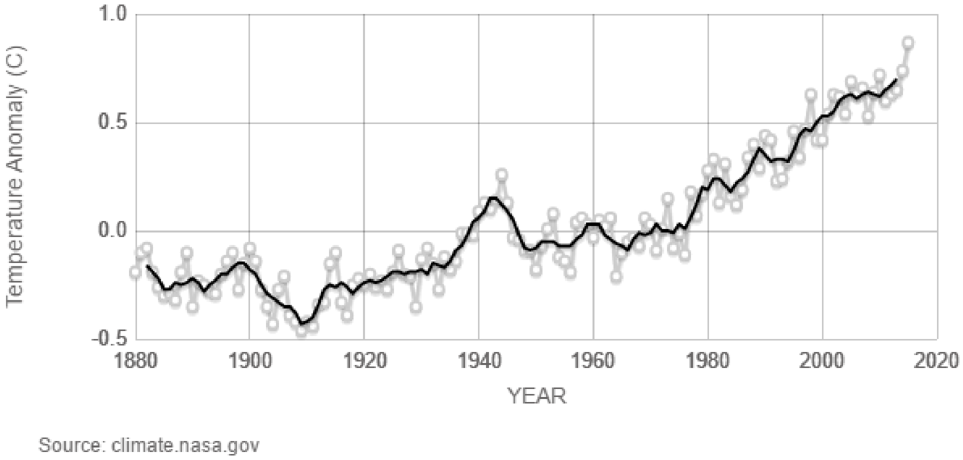

Source: climate.nasa.gov

Figure 2. The relative change of global surface temperature to 1951-980 average temperature (“Global Temperature”, 2015).

Since the levels of CO_2 concentration released into the atmosphere have enhanced annually resulting in an increase in global temperature obviously, the issue of CO_2 emission is great concerned (Sun et al., “Coal Conversion and utilization for reducing CO_2 emissions from a power plant”). CO_2 has a high positive radiative forcing of 1.66 w/m^2 (Galhotra and Grassian, 2010). Radiative forcing is the measurement of the change in the balance between radiation coming into the atmosphere and radiation going out, hence contributing to climate change. If its value is positive, warming the atmosphere, on the contrary, a negative value results in cooling of the atmosphere. For this reason, the large amount emissions of CO_2 into the atmosphere are possible to warm the surface of the Earth. Besides, CO_2 has a long lifetime remaining in the atmosphere and thus it is a very considerable factor leading to global warming (Galhotra and Grassian, 2010; “Radiative Forcing”, 2011).

1.1.2 CO_2 in Natural Gas

Natural gas is a fossil fuel. It originates from the remains of sea plants and animals which were buried on the ocean floor covered by layers of soil, sand and rock. Over millions of years, they were buried deeper and deeper. These organisms were exposed to heat and pressure as a result of being highly compressed underneath thousands of meters of soil and rock. These forces transformed the once living organisms into natural gas (“What is Natural Gas?”). The worldwide usage of natural gas is about 100 trillion scf (standard cubic feet) per year. From the estimation of total energy consumption by each type of fuel in 2030, natural gas will be the third demand fuel in that year. In addition, every sector need natural gas as energy consumption such as transportation (natural gas will be consumed around 3%), industrial (37%), residential and commercial (78%), and electric power (15%). It means that natural gas will be increasingly consumed in the future because it is a clean source of energy. However, all natural gas requires some treatment before it enters the pipeline to meet pipeline specifications. The larger demand of using natural gas leads to the larger market for industrial gas separation processes (“What is Natural Gas?”). Raw natural gas consists of various components depending on the source. Generally, methane is the main composition (about 75% - 90% of total) with other light hydrocarbons, such as ethane, propane, and butane and it also contains small amount of other higher hydrocarbons. Additionally, other impurities for example water, carbon dioxide, nitrogen, and hydrogen sulfide are composed of raw natural gas (Baker and Lokhandwala, 2008). Corrosion of pipeline by acidic gases has been one of the major problem in the gas and oil industry. One of the most interested in corrosion study is CO_2 in the pipeline of gas and oil industry which can cause failure on the equipment and thus can disrupt the oil and gas production. The basic CO_2 corrosion reaction mechanisms are shown in the equations (1) and (2),

$$CO_{2(g)} \longrightarrow CO_{2(aq)} \qquad (1)$$

$$CO_2 + H_2O \longrightarrow H_2CO_3 \qquad (2)$$

From equation (2), carbonic acid is obtained and then it dissociates into bicarbonate and carbonate in two steps as in equations (3) and (4),

$$H_2CO_3 \longrightarrow H^+ + HCO^-_3 \qquad (3)$$

$$HCO^-_3 \longrightarrow H+ CO^{2-}_3 \qquad (4)$$

CO_2 corrosion is an electrochemical reaction with the overall reaction given in

equation (5),

$$Fe + CO_2 + H_2O \longrightarrow FeCO_3 + H_2 \qquad (5)$$

which is the formation of a corrosion product $FeCO_3$ (Koteeswaran, 2010). To meet the pipeline specifications for natural gases, CO_2 content should not over 2-5%, hence, the removal of CO_2 is the crucial process (Simons, 2010).

1.2 CO_2 Capture

According to various problems occur from the presence of CO_2, the strategies for CO_2 management have gained great importance in the scientific community and the public. One of the main methods for CO_2 management is the direct capture of CO_2 from the source of release (Galhotra and Grassian, 2010). Several techniques for CO_2 capture, including absorption/adsorption, membrane technologies, cryogenic separation, and other options have been introduced (Plasynski and Chen, 2000; “CO_2 Capture Methods”).

1.2.1 Chemical/Physical Absorption

Chemical absorption is an exothermic reaction between a sorbent and CO_2 at low temperature, forming a weakly bonded intermediate compound. After that, the reaction is reversed at higher temperature so called regeneration which produces the original solvent and a CO_2 stream. Chemical absorption process consists of an absorber and a stripper (desorber) where absorbent is thermally regenerated. Thence, this process is a reversible chemical reaction of CO_2 with an aqueous alkaline solvent, usually an amine. After the regeneration, a pure stream of CO_2 is sent to compress for the subsequent transportation and storage while the regenerate solvent is then sent back to the absorber. The advantages of the chemical absorption technology are that it has been commercialized for many decades, it is the most matured technology for CO_2 capture, and it is suitable for retrofitting of the existing power plant. While, many drawbacks also exist including low CO_2 loading capacity, large instrument size, high instrument corrosion rate, amine degradation by other gases mixed with CO_2 which induces a high absorbent makeup rate, and high energy consumption during high temperature regeneration. Furthermore, energy is required for compressing the CO_2 to the conditions needed for storage and operate the pumps and blowers in the process. In absorption step, the CO_2 loading capacity is limited by the quantity of the active component of the solution. If it is saturated, only a minor loading could be achieved by physical absorption in the solution. The extensively absorbents for CO_2 capture in chemical absorption are alkanolamines which their degradations cause economic, operational, and environmental problems. However, the relatively high selectivity and a relatively pure CO_2 stream could be obtained from the chemical absorption (Kothandaraman, 2010; Wang et al., 2011; Yu et al., 2012; Li et al., 2013).

Physical absorption of CO_2 into a solvent is based on Henry’s law. The solubility of CO_2 within the solvents depends both on partial pressure and temperature of feed gas. At high pressure and low temperature, CO_2 is absorbed, whereas, CO_2 is desorbed at reduced pressure and increased temperature. Generally, physical solvents have low affinity towards acid gas, hence, these solvents are favored when feed gas has high amount of CO_2 and low purity requirements in the product. Common solvents are Selexol (dimethyl ethers of polyethylene glycol) and Rectisol (methanol). The physical absorption has been broadly applied to several industrial processes such as natural gas, synthesis gas, and hydrogen production with high CO_2 contents (Wang et al., 2011; Yeo et al., 2012; Yu et al., 2012).

1.2.2 Adsorption

As the chemical absorption possesses many drawbacks, solid adsorption processes are introduced and studied to overcome the problems from the chemical absorption process. Adsorption is the process that involves the attachment of gas or liquid to the surface of a solid (active site) by either chemical or physical attraction. In physical adsorption, the molecules of gas are attracted to the surface of sorbent by Van der Waals forces with a low heat of adsorption. While, in chemical adsorption, the gas molecules undergo a chemical reaction for binding with certain sites on the sorbent and have much higher heat of adsorption as exhibited in Figure 3. Adsorbents that used for CO_2 removal include activated carbon, alumina, metallic oxides, and zeolites. The adsorbent can be regenerated by the application of heat (so called temperature swing adsorption), or the reduction of pressure (so called pressure swing adsorption). In temperature swing adsorption, the system is heated until the attached gases are released from the adsorbent bed, on the other hand, pressure swing adsorption involves reducing the pressure of the scrubber until trapped gases are driven from the adsorbent bed. The temperature swing adsorption is more time consuming and requires larger adsorbent beds compared to pressure swing adsorption (Anderson and Newell, 2004; Wang et al., 2011; Yu et al., 2012).

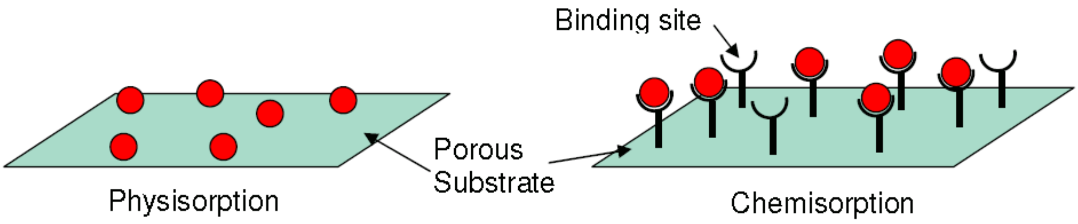

Figure 3. Physisorption and Chemisorption of CO_2 (Berger and Bhown, 2011).

1.2.3 Cryogenic Separation

Cryogenic separation undergoes the compression and cooling of gas mixtures in multiple stages to induce phase changes in CO_2 and other gases leading to gas mixture separation. Owing to the constant need for compression and refrigeration, cryogenic processes are energy intensive. It separates CO_2 from the flue gas stream by condensation, by which CO_2 condenses at -56.6°C at atmospheric pressure. This process is suitable for treating the gas streams with high CO_2 concentrations as it is complicated by contaminants. These impurities, for instance, water vapor, SO_2 and NO_x, can result in the formation of CO_2 frost and ice formation which plug equipment and simultaneously obstruct the cryogenic processes (Anderson and Newell, 2004; Wang et al., 2011).

1.2.4 Membrane Technologies

Membrane technologies have played a significant role in various environmental and energy processes e.g. CO_2 capture, natural gas sweetening, biogas upgrading, hydrogen production, etc. and can be an alternative way to the traditional methods in terms of energy requirements and economic costs. The energy efficiency and simplicity of the membrane method are attractive benefits for CO_2 capture applications. In 1961, Loeb and Sourirajan invented the first asymmetric cellulose acetate membranes. Firstly, almost researches of membranes were mainly for reverse osmosis applications. Gas separation membranes were first commercialized in 1977 when Monsanto/Perma released their hydrogen recovery system. Since the success of them and other membrane systems by Cynara, Separex and Generon led to great innovation during 1980s and 1990s for membrane materials. These development results in gas separation efficiency and membrane durability enhancement as well as making the membranes commercially competitive with the existing technologies (Scholes et al., 2008; He and Hägg, 2012).

1.2.5 Comparison between Membrane Technology and Other Methods for CO_2 Removal

The most well-known method for CO_2 removal from natural gas and in power plants is the selective physical or chemical absorption of CO_2 by a solvent (aqueous alkanolamine solutions). However, there are a lot of drawbacks in amine absorption such as corrosion of equipment, instability in the presence of oxygen, high energy consumption, high liquid losses due to evaporation of the solvent in the stripper (Simons, 2010), requires high maintenance, and expensive, thick walled and heavy absorber tower. Besides, another conventional process; adsorption process, is not also attractive because of its expensive and low efficiency, requires pre-treatment, and produces large amounts of waste water and sludge. According to these drawbacks of conventional processes, membrane technology has become a promising approach as compared to conventional processes (Yeo et al., 2012). Membrane technology plays a crucial role in economics, safety, environment and technique compared with the conventional operation (Bernardo and Clarizia, 2013). The equipment of membrane separation process is installed easily because of its modular design. The membrane technology has a high energy efficiency, low weight, a high area-to-volume ratio (Simons, 2010), and higher recovery of the desired gaseous effluent that can be reused for multiple purposes (Abedini and Nezhadmoghadam, 2010). Further, other advantages of this technique include low capital and operational cost, simple operations, environmental friendly, and low maintenance required (Yeo et al., 2012).

1.3 Membrane Technology

One example of the membrane applications is used for CO_2 capture in the natural gas process. Owing to the low energy requirements and the ease of scale-up and small size of membrane modules in off-shore installations of the membrane processes for CO_2 removal from natural gas, the solubility and diffusion of CO_2 in polymer membranes has also been received attention. Usually, membranes for CO_2 capture are incorporated with electron donor functional groups having the ability to interact with CO_2 in the feed stream, which CO_2 acts as a Lewis acid in the presence of Lewis bases (Kasturirangan, 2007).

1.3.1 Membrane Materials

Different types of membranes, for instance, common polymers, microporous organic polymers, fixed-site-carrier membranes, mixed matrix membranes, carbon molecular sieve membranes, as well as inorganic membranes, have been studied to be used in various gas separation processes. The types of materials for producing these membranes can be varied by the requirements of the process. Normally, materials are classified as inorganic and organic materials. Inorganic such as carbon nanotubes, zeolite, ceramic, metallic, metal oxide, etc. However, the membranes are mostly constructed from organic polymers; polymeric materials (Scholes et al., 2008; Ulloa, 2012).

1.3.1.1 Inorganic Membranes

Generally, inorganic membranes are made from ceramics, carbon, or metals. These membranes have been developed since 50 years ago. Because of their well-known thermal and chemical stabilities, and also higher gas permeability or selectivity when compared to polymeric membranes, inorganic membranes have been famous investigated as membranes for gas separation. For instance, zeolite and carbon molecular sieves are remarkable materials with high diffusivity and selectivity (Chung et al., 2007), and ceramic membranes are thermally stable (above 400°C) can be used to separate hydrogen from gasified coal. Basically, inorganic membranes can be divided into two types: nonporous (dense) and porous membranes. Ceramic membranes such as silica, alumina, titanium, glass, and porous metals e.g. silver and stainless steel are the examples of commercial porous inorganic membranes which have high permeabilities but low selectivities. For dense inorganic membranes, Pd metal based membranes and metal oxide membranes are specific in hydrogen separation and oxygen separation, respectively. These membranes are very specific in their separations (Abedini and Nezhadmoghadam, 2010). Nevertheless, because of the expensive and difficulty of inorganic materials to produce large membranes from their fragile structures, organic materials are more attractive due to their ease of production, reproducibility and low cost (Ulloa, 2012).

1.3.1.2 Organic Membranes

One example of organic membranes, Schell and co-workers in 1989 reported advances in cellulosic membranes for gas separation. Cellulose acetate membranes have been used commercially for many gas separation applications, most of which contain either hydrocarbon or polar. The main gas separation applications for cellulose acetate membranes are carbon dioxide removal from natural gas (Schell et al., 1989). Moreover, many principal suppliers of membrane for natural gas separation also use cellulose acetate as a membrane's material for CO_2 separation as presented in Table 1 (Baker and Lokhandwala, 2008).

Table 1. Some of principle membrane suppliers (Baker and Lokhandwala, 2008).

Company	Principal natural gas separation	Membrane material
Medal (Air Liquid)	CO_2	Polyimide
W.R. Grace	CO_2	Cellulose acetate
Separex (UOP)	CO_2	Cellulose acetate
Cynara (Natco)	CO_2	Cellulose acetate
ABB/MTR	CO_2, N_2, C_3+ hydrocarbons	Perfluoro polymers silicone rubber
Permea (Air Products)	water	polysulfone

Also, other polymeric materials have been accepted as membrane materials continuously due to polymeric materials are easy to operate and scale up, low production cost, light in weight, capable to modify the structure of membrane, processable into high surface area membrane, and able to be used in a variety of applications (Moore and Koros, 2005; Cong et al., 2007; Wang and Han, 2012). This type of membrane could be fabricated in different geometries depending on the application. Generally, flat-sheet membranes are simple to produce and can be used in a plate-and-frame or spiral-wound shape. In case of hollow fiber membranes, an extrusion process would be required with specialized machinery and strict quality control (Ulloa, 2012). Morphology of polymeric membranes is illustrated in Figure 4.

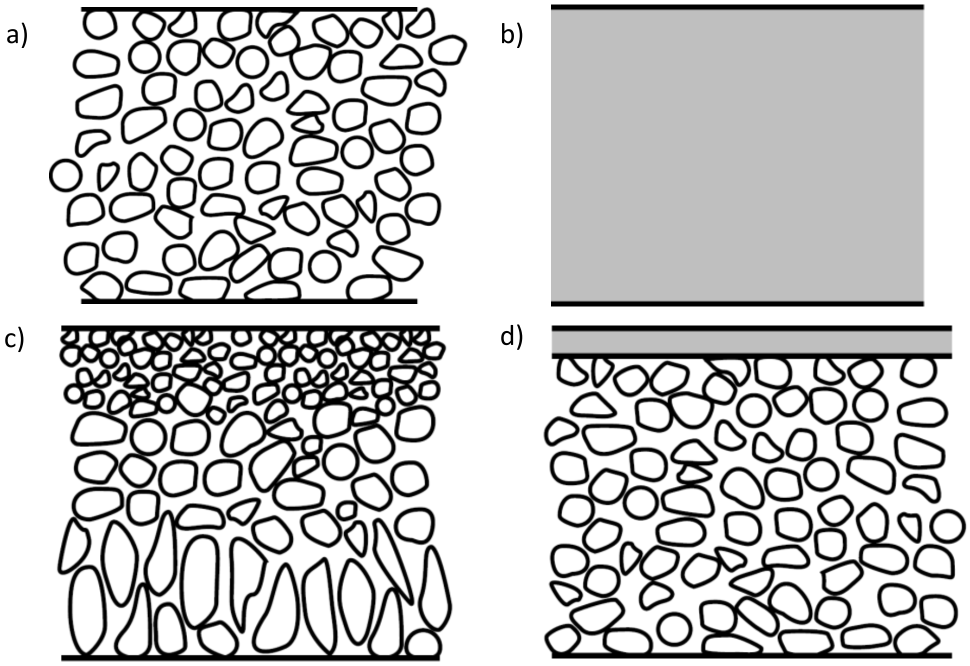

Figure 4. Morphologies of polymeric membranes; symmetrical membranes are the two-top illustrations, a) microporous membrane and b) non-porous dense membrane, while asymmetric membranes are the two-bottom illustrations, c) Loeb-Sourirajan membrane and d) thin-film composite membrane.

In case of symmetrical membranes, they have uniform morphology, can be divided into microporous and non-porous dense membranes as shown in Figure 4(a) and 4(b). Porous in microporous membranes allow the separation by the passage of smaller penetrants, while non-porous dense membranes allow the penetrants by solution-diffusion through the membranes which is governed by the chemical interactions between the polymer and the penetrant. Alternatively, asymmetrical membranes divided into Loeb-Sourirajan membranes and thin-film composite membranes as shown in Figure 4(c) and 4(d). These membranes consist of a thin and also selective layer overtop a microporous support layer. These support layer should be porous enough so as not to hinder the transport of penetrants and also rigid enough to endure the driving forces of the separation. Loeb-Sourirajan membranes are formed by a controlled precipitation of a polymer out of solution, creating a thin selective layer (500-2000 A° thick) and a microporous substructure (50-200 μm thick) out of the same material. For fabrication of composite membranes, other polymers are coated as thin layer on the top of microporous support layer (Ulloa, 2012).

Several researchers have been fabricated the organic membranes and examined their abilities to separate gas mixture. Xing and Ho (2009) prepared crosslinked polyvinylalcohol (PVA)/polyethyleneglycol (PEG) blend membranes for CO_2/CH_4 separation. They could achieve high CO_2/CH_4 selectivity for this membrane as a result of the polar segments in the membrane. The CO_2 permeability of 80.2 Barrers and a CO_2/CH_4 selectivity of 33 at 30 °C. Lin and Freeman (2006) determined the permeability of cross-linked poly(ethylene glycol diacrylate) to He, H_2, O_2, N_2, CO_2, CH_4, C_2H_4, C_2H_6, C_3H_6, and C_3H_8. The polar units in PEO could react with CO_2 molecules which resulted in high solubility selectivity for CO_2/nonpolar gas pairs. Hence, it is unsurprised that CO_2 is the most permeable penetrant in their study. In 2008, swollen chitosan membranes have been studied by El-Azzami and Grulke (2008) for CO_2 separation from H_2 and N_2 at 20–150 ˚C and feed pressure range of 1.5–5 atm. The best results in their works are obtained at 110 ˚C and 1.5 atm. The CO_2 permeability of 482 barrers, the CO_2/H_2 selectivity of 43.4, and the CO_2/N_2 selectivity of 250 at 110˚C. Later on, Francisco et al. (2010) fabricated diethanolamine-impregnated poly(vinyl alcohol) membranes for CO_2 separation from N_2 application by varying the amount of diethanolamine 0 wt.% to 50 wt.%. They found that the membrane containing 20 wt% diethanolamine exhibited the best performance among all the membranes. At higher temperature and lower CO_2 partial pressure, the higher selectivity can be obtained from these membranes. In addition, they also concluded that these membranes exhibited a CO_2 permeance of 9.7 GPU and a CO_2/N_2 selectivity of 112, which achieved from the mixture containing 15.6 mol%CO_2 at a feed pressure of 308 kPa and ambient temperature.

Nevertheless, organic membranes can also be produces from other biomaterials of natural resources as follows;

- Cellulose

Cellulose is the natural polymer (polysaccharide) which is the most abundant material in the world, synthesized by plants, algae and also some species of bacteria (Legnani et al., 2008), thereby, it is a biodegradable material. From the structure of cellulose, there are the strong hydrogen bonds between cellulose chains, hence, cellulose does not melt or dissolve in ordinary solvents (Wu and Yuan, 2002). Although, cellulose produced from plant is chemically the same with that one produced from bacteria (β-1,4-glucans), the degree of polymerization (13,000 to 14,000 for plant cellulose and 2000-6000 for bacterial cellulose), structure, and some properties are different (Jonas and Farah, 1998). Therefore, among other polymers, cellulose has been one of the most studied as a membrane material due to its abundance and high mechanical strength (Thiyam et al., 2015). In 1970, Gantzel and Merten studied the permeability of cellulose acetate membranes. They suggested that these membranes could be applied in the gas separation process as the permeation rate of each gases are different (Gantzel and Merten, 1970).

Cellulose acetate (CA) membrane and cellulose acetate-TiO_2 nanoparticle composite membrane were synthesized to investigate CO_2 adsorption by Hafeez et al. (2015).The theoretical steps of CO_2 adsorption in membranes and on TiO_2 nanoparticles blended in CA matrix are as follows: (1) transportation of gas molecules from bulk phase near the surface of membrane, (2) diffusion of gas molecules into the external surface of membrane, and (3) gas molecules solubilize in membrane and adsorb in polymeric chains and on TiO_2 nanoparticles. They found that CO_2 was adsorbed in both membranes but the blended membranes achieved higher CO_2 adsorption capacity. They mentioned that the addition of TiO_2 nanoparticles could not only increase the free volume between polymeric chains, which may be helpful in diffusion and adsorption of CO_2, but also provides OH functional groups that enhances CO_2 adsorption. Also, ester groups of CA matrix help to improve the CO_2 affinity. Another important aspect for gas and polymer interaction is polarity that have affected the CO_2 adsorption capacity. As CO_2 has quadrupole moment, it is able to soluble in polar polymers and its polar bonds have strong interaction with OH groups of TiO_2. Recently, Venturia et al. (2016) analyzed the behavior of Microfibrillated cellulose (MFC) films and their blends with PVAm (Polyvinylamine) in views of their uses in CO_2 separation applications. The membranes were obtained by casting from a solution of carboxymethylated MFC and Lupamin. The films were subjected to a thermal treatment in a vacuum oven in order to improve the film stability at high humidity by decreasing water uptake and possibly creating covalent bonding through the fibers and the polymer. Gas permeation of CO_2 and CH_4 were performed at 35°C as a function of relative humidity and water sorption.

From their results, they suggested that both MFC and MFC-Lupamin films have attractive ability for CO_2/CH_4 separation providing very high selectivity values (more than 400) which achieved separation performance well above the trade-off of 2008 Robeson's plot. On the other hand, they claimed that the difference between CO_2 and CH_4 permeability reduced leading to a strong decrease of selectivity when the relative humidity exceed 60%.

- *Bacterial Cellulose*

Bacterial cellulose is produced by Gram-negative bacteria (*Gluconacetobacter xylinus*), which shows several unique properties when compared to plant cellulose (Legnani et al., 2008). This aerobic Gram-negative bacteria is active when fermented at pH 3-7 and temperature range 25 to 30°C using saccharides as carbon source (Esa et al., 2014). The formation of cellulose occurs at the interface between air and cellulose pellicle, hence, oxygen is an important factor for the production of cellulose.

Biochemical pathway for cellulose formation from glucose is shown in Figure 5. When cellulose produced, the pores presented in the form of fibrils and then those synthesized fibrils formed together into a ribbon of crystalline cellulose. The self-assembly process might be called crystallization, which occurred after the polymerization of the fibrils was completed.

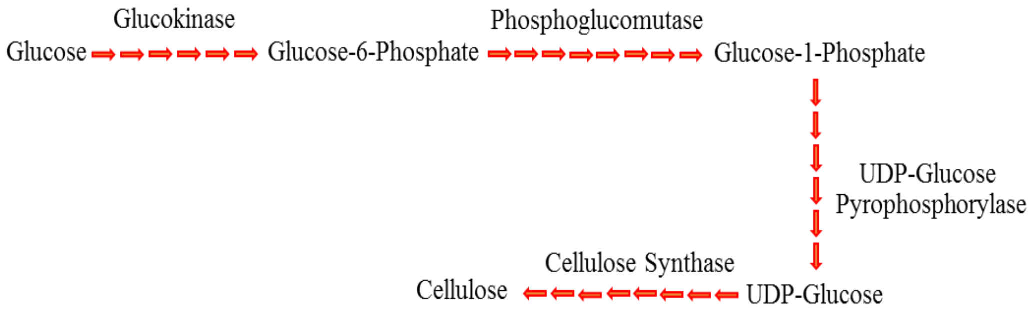

Figure 5. Biochemical pathway for cellulose synthesis in Acetobacter xylinum (Jonas and Farah, 1998).

Bacterial cellulose consists of glucose molecules linked by β(1→4) - glycosidic bonds with molecular formula $(C_6H_{10}O_5)_n$ forming linear chains. These chains are held together by inter- and intra- hydrogen bonding as demonstrated in Figure 6 (Albu et al., 2014; Esa et al., 2014). Bacterial cellulose is normally of crystallinity structure. The 3D structure of an ultrafine network of cellulose nanofibers (3-8 nm) which is called "nanocelluloses" could be obtained from the culture medium (Legnani et al., 2008) resulting in formation of hydrogel sheet with high surface area and porosity. Microfibrils of bacterial cellulose are about 100 times smaller than those of plant cellulose. The abundant surface of hydroxyl groups of the cellulose formed makes it hydrophilic, biodegradable, and chemical-modifying capable (Esa et al., 2014).

Bacterial cellulose membrane appearance is gelatinous and transparent. The remarkable properties of bacterial cellulose include high molecular weight and crystallinity (60-90%), high mechanical strength, high purity (free of lignin and hemicellulose), and high water-holding capacity. In addition, this membrane has unique properties such as nanometric structure, physical and mechanical properties which lead to a great number of applications (Legnani et al., 2008) such as dietary fiber, acoustic or filter membrane, ultra-strength paper, and reticulated fine fiber network with coating, binding, thickening, and suspending (Keshk, 2014). For example, in 2008, Legnani et al. fabricated dried bacterial cellulose membranes as flexible substrate for organic light emitting devices (OLED) by depositing Indium tin oxide (ITO) film onto bacterial cellulose membranes. They concluded that this membrane is possible to use as flexible substrate to develop a fully biocompatible OLED (Legnani et al., 2008). Additionally, the application of bacterial cellulose can be applied instead of cellulose from plants in areas that plant cellulose hardly be used because of its high purity and crystalline structure (Jonas and Farah, 1998).

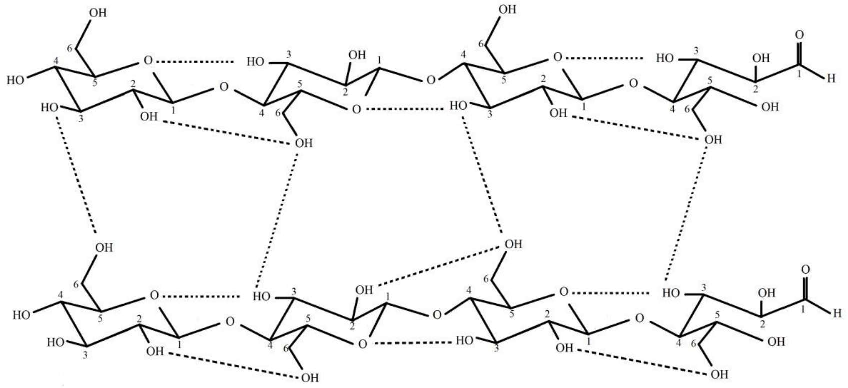

Figure 6. Inter- and intra-hydrogen bonding of bacterial cellulose (Esa et al., 2014).

Bacterial cellulose may be considered as an ideal hydrophilic matrix for impregnating nanoparticles. In 2009, Hu et al. prepared bacterial cellulose membranes incorporated with silver chloride nanoparticles by immersing the membranes in silver nitrate solution and sodium chloride solution. After that, the synthesis of silver chloride nanoparticles in the three-dimensional non-woven network of bacterial cellulose nanofibrils occurred (Figure 7). Due to the nanoporous structure and high oxygen (from ether and hydroxyl) density of bacterial cellulose fibers, it is an effective nanoreactor for nanoparticles synthesis. These nanopores are important for introduction of silver ions. After the impregnation of silver chloride nanoparticles, bacterial cellulose membrane exhibited high hydrophilic property and strong antimicrobial activity against both S. aureus (Gram-positive bacteria) and E. coli (Gram-negative bacteria) that are found on the contaminated wound, so this membrane can be applied to wound dressing.

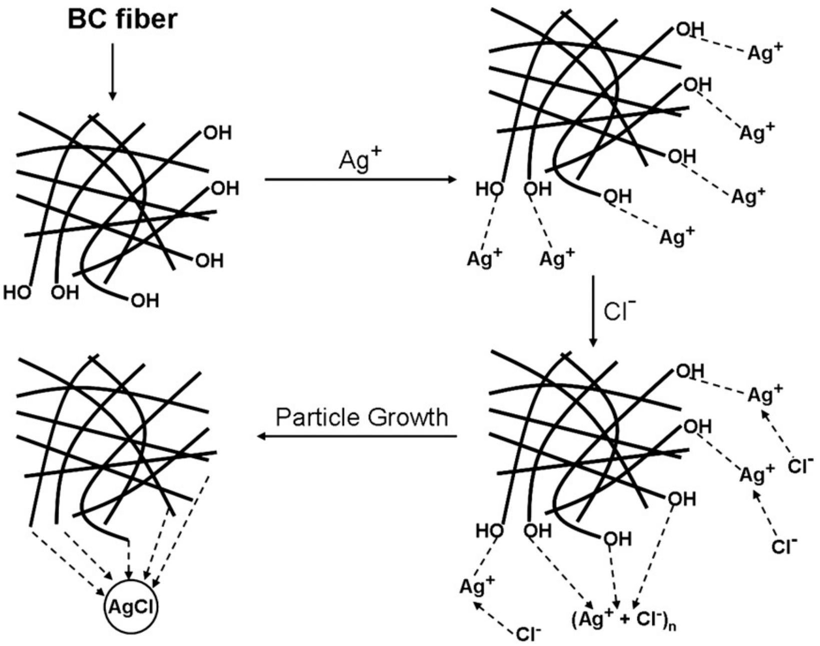

Figure 7. Schematic representation of the formation mechanism of AgCl nanoparticles (Hu et al., 2009).

Additionally, bacterial cellulose is extremely abundant and of low cost, thereby, blending it with other polymers, for instance, chitosan, poly (ethylene glycol) (PEG), and gelatin via immersing wet bacterial cellulose pellicle into chitosan, PEG, or gelatin solutions and then freeze-drying step is needed. The products look like a foam structure that used for potential biomedical application of tissue engineering scaffold and wound-dressing material (Keshk, 2014).

In order to improve bacterial cellulose's ability for CO_2 capture application, modified it with silk fibroin is hopeful to be a useful method to introduce amino acid groups into cellulosic materials (Shang et al., 2011). The amide bonds of the protein may act as electron donor functional groups i.e. accessible sites for interaction with CO_2 molecules, resulting in enhancement of CO_2 capture (Lin and Park, 2011). Further, silk fibroin has already been used for improving the mechanical properties of the bacterial cellulose films (Jung and Jin, 2007) and for fabrication of bacterial cellulose based sponge scaffolds for tissue regeneration (Oliveira Barud et al., 2015).

- Silk Fibroin

Silk fibroin is a fibrous protein produced by the domestic silkworm *Bombyx mori*, which provides structural roles in cocoon formation, that has been used as films, three-dimensional scaffolds, electrospun fibers, and microspheres a long time due to their superior mechanical properties, favourable oxygen permeability, high thermal stability, and also versatile protein biomaterial (Tudora et al., 2013). The structure of silk cocoon, which two fibroin filaments join together and are formed in one *Bombyx mori* silk filament where sericin coats the silk fibroin and acts as an adhesive (Shang et al., 2013), is shown in Figure 8. Sericin is a group of glycoproteins (nonfilamentous protein, gum-like protein) that covered the surface of fibroin. The amount of sericin is about 25-30% of the total silkworm cocoon by weight (Rockwood et al., 2011).

Silk fibroin consists of a light chain (its size is much smaller than heavy chain) and a heavy chain of proteins linked by a single disulfide bond (Tudora et al., 2013). The heavy chains form discrete β-sheet crystalline structure serving as the main structural component, whereas, the light chains are not associated with the formation of the crystalline region in silk fibroin (Koh et al., 2015). The molecular structure of silk fibroin heavy chain composes of 12 hydrophobic amino acids, which segregated by 11 hydrophilic regions (Tudora et al., 2013; Koh et al., 2015).

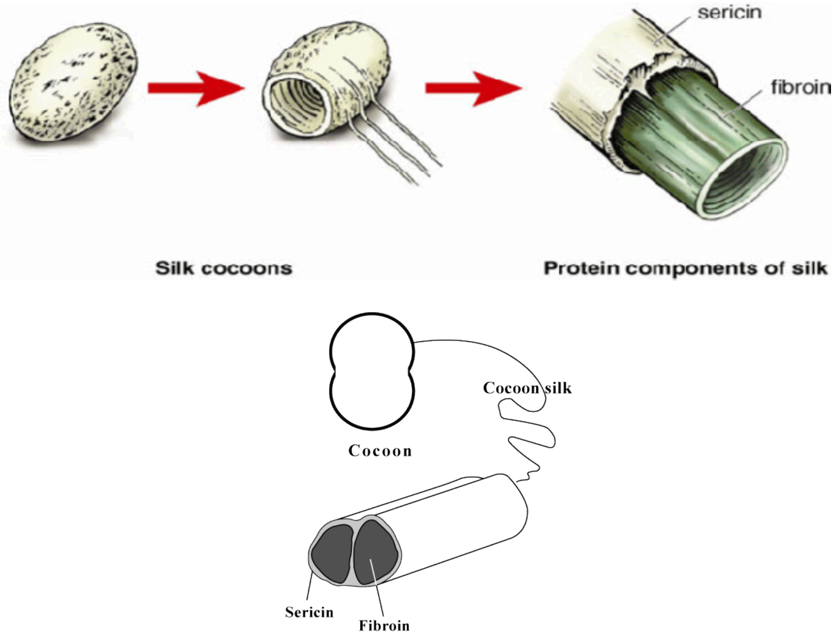

Figure 8. Structure of silk cocoons (Bunnell, "Silk Fibroin"; "Structure of cocoon silk").

There are three main conformations of silk proteins, including α-helical and random coil structures ascribed to silk I structure, while β-sheets to the silk II structure, which the amount of β-sheet is about 50% in case of *Bombyx mori* silk corresponding to the proportion of the $(\text{Gly-Ala})_n$ motif. Thereby, *Bombyx mori* silk fibroin is accepted that it is composed of a highly repetitive $(\text{Gly-Ala})_n$ sequence motif leading to antiparallel β-sheet conformation that is silk II of the crystalline form (Liu and Zhang, 2014). The amino acid sequence, $(\text{Gly-Ser-Gly-Ala-Gly-Ala})_n$, is the main component in its primary structure as presented in Figure 9. The tight packing of the sheets results from the high content of glycine that leads to the rigid structure and higher tensile strength of silk. Therefore, the combination of stiffness and toughness of silk allow it to be a material with many applications in several areas.

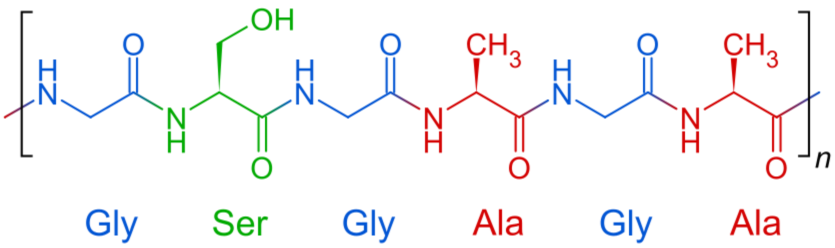

Figure 9. The amino acid consequence of silk fibroin (“Fibroin”, 2015).

Yang et al. (2000) prepared and examined the blend membranes between cellulose and silk fibroin. From their results, these blend membranes which obtained by coagulating with acetone-acetic acid were miscible and had a strong hydrogen bond interaction exists between cellulose and silk fibroin. Moreover, they found that the specified intermolecular hydrogen bonds between OH at the C2, C3 position of cellulose and NH in the amide groups of silk fibroin increased, which affected to the decreasing of the intramolecular hydrogen bonds of cellulose.

1.3.1.3 Composite Membranes

The segmental flexibility of polymeric membranes leads to limit their ability especially when use at high temperature. While, inorganic membrane materials are difficult and expensive to fabricate large membranes due to their fragile structures. For this reason, polymeric membranes are still attractive. Also, to provide a solution to the trade-off problem of polymeric membranes, polymer-inorganic nanocomposite materials; defined as inorganic nanofillers dispersed in a polymer matrix, have been investigate for gas separation. Polymer composites could enhanced material properties compared to pure polymers. The nanocomposite materials offer the advantages from both materials such as the flexibility and processability of polymers, and the selectivity and thermal stability of the inorganic fillers. This composite membrane could thus improve membrane performance for gas capturing or separation purpose. The blended components in a composite membrane thus provide a high capability to adsorb the desired gas. The addition of inorganic nanofillers may affect the gas separation in either the interaction between polymeric chain segments and nanofillers or the interaction between hydroxyl and other functional groups on the surface of the inorganic phase with polar gases e.g. CO_2. This could obstruct the polymeric chain packing resulting in an increase in the free volumes between the polymeric chains and thus enhance gas diffusion and concurrently improve the gas solubility (Cong et al., 2007; Hafeez et al., 2015; Oliveira Barud et al., 2015). The nanocomposite membranes can be divided into two types by their structure: (a) polymer and inorganic phases connected by covalent bonds and (b) polymer and inorganic phases connected by van der Waals force or hydrogen bonds as shown in Figure 10.

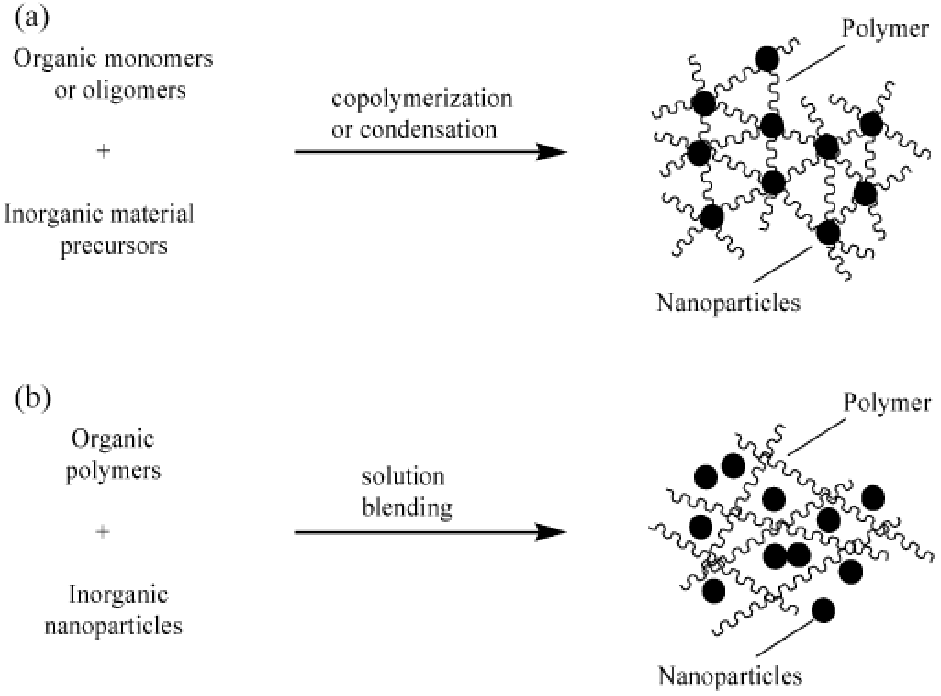

Figure 10. Polymer-inorganic nanocomposite membrane’s types; (a) polymer and inorganic phases connected by covalent bonds and (b) polymer and inorganic phases connected by van der Waals force or hydrogen bonds (Cong et al., 2007).

- Zinc Oxide Nanoparticles

Zinc oxide (ZnO) nanoparticles have their own important properties, hence, they have been used in large area of applications e.g. gas sensor, chemical sensor, bio-sensor, optical and electrical devices, cosmetics, solar cells etc. (Djurisic et al., 2012). ZnO-containing material can be developed to apply in CO_2 adsorption process as CO_2 is sensitive to the oxide surface structure. In 1982, Lavalley et al. examined the CO_2 adsorption on ZnO surface using FTIR spectroscopy. They revealed the particular sites for CO_2 adsorption on ZnO surface were Zn^{2+} ions with two vacancies and a reactive oxygen ion in an adjacent position as the below figure (Figure 11). They also claimed that this adsorption leads to an increase of Lewis acidity of the coordinatively unsaturated cations.

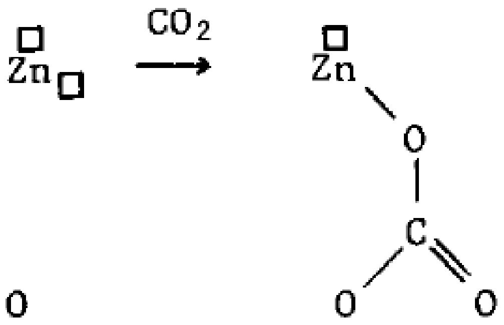

Figure 11. CO_2 adsorption on ZnO surface (Lavalley et al., 1982).

Reactions of CO_2 on ZnO surface were also investigated by Galhotra and Grassian (2010). They mentioned that the possible ways for CO_2 adsorption could be the formation of chemisorbed products and also physisorbed bent CO_2 as suggested by the peak at 2350 cm^{-1} that is assigned to the asymmetric stretching mode (υ_3) of CO_2 the ZnO surface reacts with carbon dioxide to form bent CO_2, bicarbonate, carbonate and carboxylate species under dry conditions as presented in Figure 12.

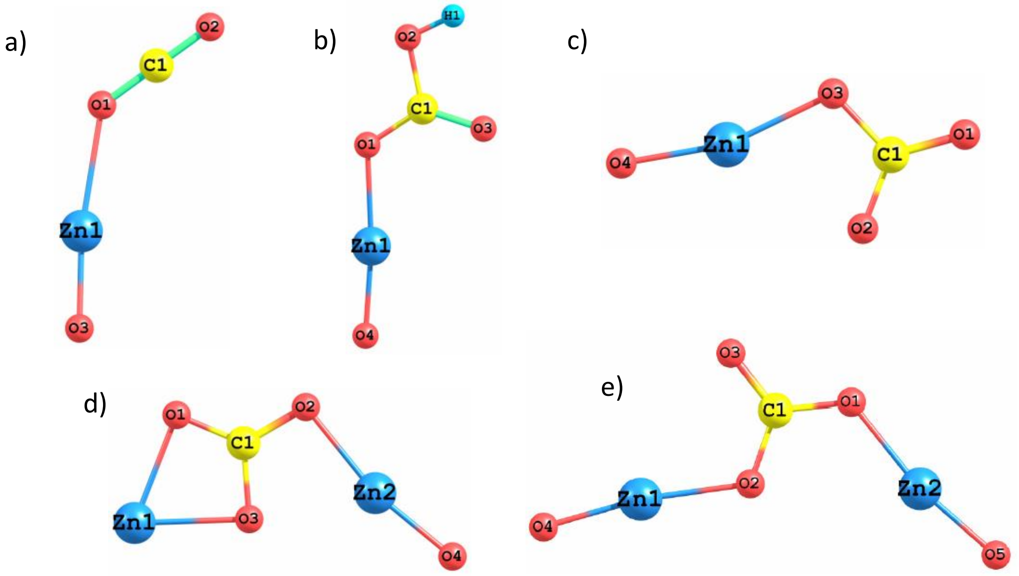

Figure 12. Structure of (a) bent CO_2; (b) bicarbonate; (c) monodentate carbonate; (d) bidentate carbonate; and (e) carboxylate formed on the ZnO surface (Galhotra and Grassian, 2010).

Later on, Tang and Luo (2013) studied the adsorption of CO_2 molecules on five different ZnO surfaces, including $(000\bar{1})$, (0001), $(10\bar{1}0)$, $(11\bar{2}0)$, and $(11\bar{2}1)$ surfaces, by using the density functional theory plus U (DFT+U) method. On the basis of their surface energy calculations, the stability of different ZnO surfaces was revealed, which was in the sequence of ZnO$(10\bar{1}0)$ > ZnO$(11\bar{2}0)$ > ZnO$(000\bar{1})$ /ZnO(0001) > ZnO$(11\bar{2}1)$. Therefore, both types of surfaces $(10\bar{1}0)$ and $(11\bar{2}0)$ are exposed and most likely to be found, moreover, they also concluded that there are abundant $(10\bar{1}0)$ and $(11\bar{2}0)$ faces on ZnO nanoparticles. According to their results, the preferred CO_2 adsorption state on ZnO surfaces depends strongly on the nature of the substrate. Figure 13 shows all of possible molecular orientations for adsorption modes on each considered surfaces, including monodentate, bidentate, and tridentate geometries. The CO_2 molecule maintained its linear structure during adsorption on $(000\bar{1})$ and (0001) surfaces as shown in Figure 14(a) and 14(b), where they are O-terminated and Zn-terminated facets, respectively. Hence, it was the physisorption owing to the lacking of coordinatively unsaturated Zn-O dimers, which are needed for CO_2 to be activated, and also could not support the CO_2-surface interaction. In contrast, the adsorption on the mixed-terminated $(10\bar{1}0)$, $(11\bar{2}0)$, and $(11\bar{2}1)$ planes demonstrated the chemisorption and resulting activation of CO_2. For the ZnO $(10\bar{1}0)$and ZnO $(11\bar{2}0)$ planes, CO_2 preferred to bind with two neighboring surface Zn atoms by its two O ends and C atom with a lattice O atom as presented in Figure 14(c) and 14(d), thus leading to a tridentate carbonate species. In case of ZnO $(11\bar{2}\bar{1})$ plane, a stable bidentate carbonate was found upon exposure to CO_2 (Figure 14(e)). The binding of CO_2 to ZnO surfaces was strengthened in the order of ZnO $(000\bar{1})$ ≤ ZnO (0001) < ZnO $(11\bar{2}1)$ < ZnO $(11\bar{2}0)$ ≤ ZnO $(10\bar{1}0)$. They mentioned that the ZnO $(10\bar{1}0)$ facet was not only the most stable but it was also the best site for CO_2 adsorption on ZnO particles. In case of the chemisorbed CO_2 with ZnO surfaces, the 2p states of the CO_2 were able to overlap with the relevant 2p orbitals of surface oxygen and 4s orbitals of surface zinc. The mechanism presented as follows: Zn donated electron to the antibonding orbitals of CO_2 and CO_2 bonding orbital back-donated electron to lattice O resulting in elongated C=O internal bond distances as well as a rather bent O=C=O angle.

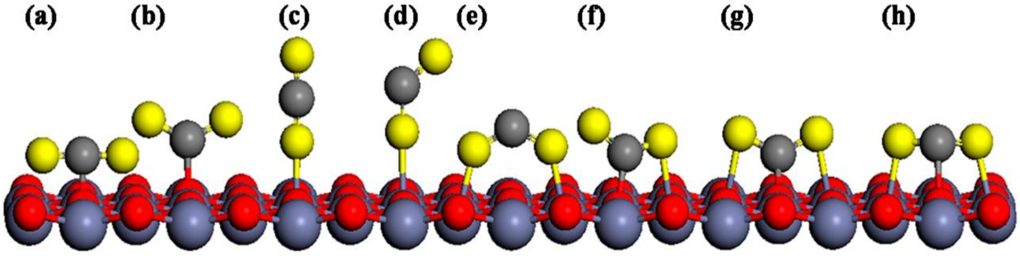

Figure 13. Possible molecular orientations; (a−d) monodentate, (e, f) bidentate, and (g, h) tridentate adsorption modes for CO_2 on ZnO surfaces as represented by a ZnO $(000\bar{1})$ surface. Carbon atom, adsorbate oxygen, lattice oxygen, and zinc represented by dark gray, yellow, red, and blue spheres, respectively (Tang and Luo, 2013).

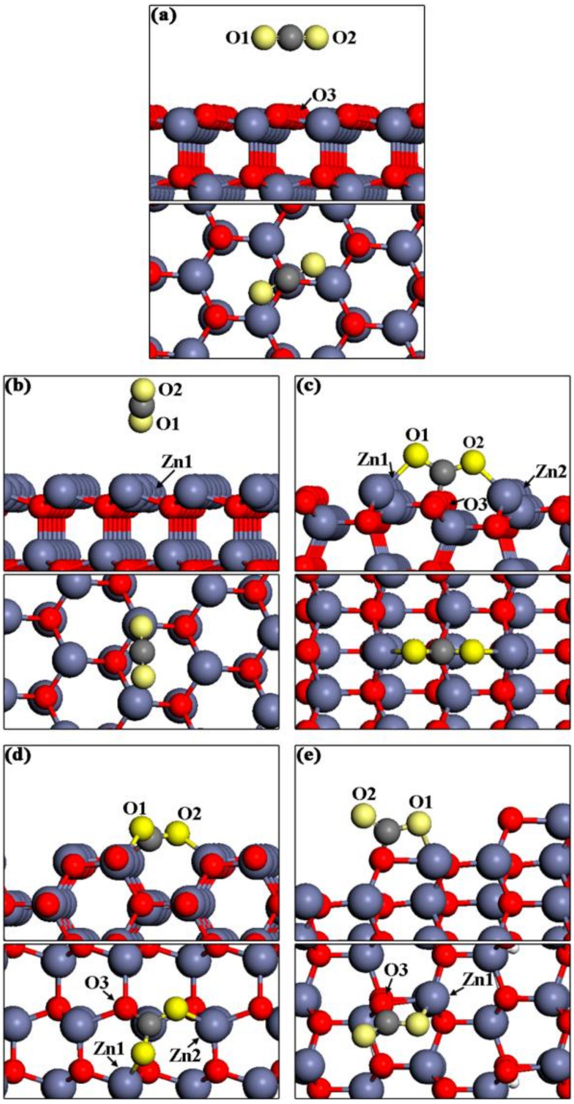

Figure 14. Most energetically favorable configurations for adsorbed CO_2 on (a) ZnO (000$\bar{1}$), (b) ZnO (0001), (c) ZnO (10$\bar{1}$0), (d) ZnO (11$\bar{2}$0), and (e) ZnO (11$\bar{2}$1). Atoms engaged in the adsorbate-substrate interaction were labeled. Upper panels show side views, while lower panels indicate top views. Carbon atom, adsorbate oxygen, lattice oxygen, and zinc represented by dark gray, yellow, red, and blue spheres, respectively (Tang and Luo, 2013).

Furthermore, Farias et al. (2013) studied the physical adsorption of CO_2 on the (0001) and (000$\bar{1}$) surfaces, and the chemical adsorption of CO_2 on the (0001) surface by using the density function theory (DFT). The valence states of O were $2s^2$, $2p^4$; of Zn were $3d^{10}$, $4s^2$; and of C were $2s^2$, $2p^2$. They presented the geometry optimization results for the CO_2 physical adsorption on (0001) and $(000\bar{1})$ surfaces, where the large distance between CO_2 and ZnO surface was noticed owing to the physical process. According to their Electron localization function (ELF) analysis, CO_2 molecule had insignificant interaction with (0001) and $(000\bar{1})$ surfaces in physical adsorption. Additionally, from their results of ELF analysis for the chemical adsorption with bidentate and tridentate species, it pointed out a covalent bonding between CO_2 and the (0001) surface in both adsorptions.

1.3.2 Study of the Interaction of Membrane Materials with CO_2 by FTIR Spectroscopy

Every atom in molecules vibrate continuously with respect to each other at temperature above absolute zero. When the frequency of a specific vibration is matched with the frequency of the IR radiation directed to the molecule, that molecule absorbs the radiation and the associated energy is converted into some type of motion leading to absorption bands observed in the mid IR region. FTIR spectroscopy provides the absorption bands at the specific frequency of the sample absorbs the radiation, which allows to identify the chemical functional groups of the sample (qualitative analysis), and the intensity of the absorptions (quantitative analysis) that related to the concentration of the component. For instance, Kasturirangan (2007), they split IR beam into two paths, one path is used to measure the υ_2 frequency spectra regions of the polymer film in the presence of CO_2 and another path is used to measure the spectrum of CO_2 in the absence of the film. The information about the interactions of CO_2 with any polymer could be achieved by the differences in these two spectra. In their work, they revealed the specific CO_2-polymers containing C=O and C-F groups interactions using *in situ* FTIR spectroscopy. They claimed that the longer alkyl chains connected to the C=O group could improve the interactions possibly by the formation of cooperative C-H…O bonds that further stabilize the Lewis acid-base complex between C=O and CO_2 and the chain branching could enhance the accessibility of C=O group and thus favors interaction with CO_2. For example, PBMA has longer alkyl side chains attached to the C=O group and hence it has a higher free-volume than PMMA. According to PBMA structure, the Lewis acid-base interactions are favored because it is more accessible for electronic sharing with CO_2. In case of Polyvinylidene fluoride

(PVDF), the electron rich fluorine atoms act as Lewis base or electron donor, which provide the strong interactions between C-F…CO_2 groups, even though, it is absent of chain branching and lower free-volume. Nevertheless, there was no shifted in IR spectra were noticed for Polystyrene (PS) that indicated the absence of Lewis base groups in the backbone. Thereby, they suggested that these results proved molecular level evidence for the CO_2 interactions with C=O and C-F groups.

In addition, Kazarian et al. (1996) investigated the specific interactions of CO_2 with polymer films via using Fourier Transform IR spectroscopy to observe whether the bending mode of CO_2 (range of 680-600 cm^{-1}) changed when the basic functional groups contained polymers incorporated with CO_2. PMMA film was subjected to CO_2 41-83 bars for 1 h and then the pressure was released. They found three main peaks; 667, 662, and 654 cm^{-1} appeared. However, after removing CO_2 gaseous, the peak at 667 cm^{-1}, which arose from free and unassociated CO_2, was not presented, there was just only the 662 and 654 cm^{-1} bands that appeared as peaks on the broad band shifted to lower frequency from the gaseous CO_2, indicating the CO_2 molecules remaining in the polymer film. They mentioned that these new bands were of the out-of-plane and in-plane bending modes of CO_2 interacting with the carbonyl of PMMA, while the larger shift was the in-plane mode (654 cm^{-1}). These shifts and splitting peaks provided strong evidence for the specific interactions between CO_2 and PMMA, most probably by the Lewis acid-base interaction, where electron donating from lone pair of the oxygen atom of the carbonyl group of the polymer to carbon atom of CO_2 molecule that acts as electron acceptor. CO_2 molecules also has a considerable quadrupole moment which they could not entirely exclude the contribution of electrostatic forces in the interaction of CO_2 with PMMA. Additionally, they also examined the IR spectra of asymmetric stretching mode of CO_2 entrapped in the PMMA film. Only a band at 2338 cm^{-1} and a weak low-frequency band at 2326 cm^{-1} were noticed. They suggested that there was only one type of the site within the polymer matrix for CO_2 molecules for their conditions because if there were more sites for CO_2 within the matrix, it should have more than one band in the asymmetric stretching region. On the other hand, they did not find any splitting and shift for the polymers lacking electron-donating functional groups.

Afterward, Nalawade et al. (2006) also used a Fourier transform-infrared spectroscopy (FT-IR) to determine the intermolecular interactions between CO_2 and polymers having different functional groups along the main chain, which are ester, ether, and aromatic ring of polyesters, poly(ethylene glycol) (PEG), and polyphenylene oxide (PPO), respectively. The absorption bands were expected to be observed the significant changes in their study due to the interaction Lewis acid-base between CO_2 and polymers. They claimed that the shift of FTIR absorption bands of the polymer is an indicator of interaction between polymer and CO_2, however, it is only on a qualitative level. They found the slightly shifted to higher wavenumbers of the both C-O stretching vibrations and the aromatic C-H bending vibrations in the presence of CO_2 because of the formation of complexes between CO_2 and these functional groups. Besides, the extra bands of CO_2 bending vibrations of PPO under CO_2 condition were observed compared to the single band of CO_2 at 667 cm^{-1}. For aromatic polyesters (P120 and P130), they focused on the carbonyl group and aromatic ring as the sites that can react with CO_2. The stretching vibrations of the carboxyl group (C-O, around 1720 cm^{-1}) were also shifted to higher wavenumbers, maximum shifts of 3.7 for P120 and 2 cm^{-1} for P(130). While they found the aromatic absorption region 730 cm^{-1} was shifted to lower wavenumbers. They mentioned that there were interactions of CO_2 with the Lewis base sites and the phenyl rings available in polyesters. In case of PEG, the ether group (C-O) was able to interact with CO_2. A shifted of the C-O stretching mode was noticed. Furthermore, the bending vibration of CO2 entrapped in PEG demonstrated a very broad spectrum and also the splitting of a band because of weak interactions between CO_2 and the ether group. If they rank the interaction strength with CO_2 by the band width of CO_2 bending vibrations, they could obtain the higher in the polymers containing ether group (higher band width) than the polymers containing ester group.

1.4 Lewis Acid-Base Interactions

Lewis acid-base interaction is the interaction between a Lewis acid, an electron pair acceptor, and a Lewis base, an electron pair donor, by which Lewis base donates electron pair to Lewis acid leading to form a new sigma bond to the electron deficient center in the acid. The Lewis acid is sometimes referred to as electrophile, on the other hand, the Lewis base is referred to as nucleophile (“Introduction to Lewis acid-base chemistry”). Table 2 presents examples of Lewis acids and bases.

Table 2. Examples of Lewis acids and Lewis bases ("Preparation and reactions of carboxylic acids").

Lewis Acid	**Lewis Base**
Lewis Acids: Electron pair/lone pair acceptors Lewis Acids are Electrophilic.	Lewis Bases: Electron pair/lone pair donors Lewis Bases are Nucleophilic.
Examples: • All cations are Lewis acids since they are able to accept electrons (e.g. Cu^{2+}, Fe^{2+}, etc.) • An atom, ion, or molecule with an incomplete octet of electrons can act as an Lewis acid (e.g. BF_3, AlF_3) • Molecules that have multiple bonds between two atoms of different electronegativities (e.g. CO_2, SO_2)	Examples: • Simple anions (e.g. OH^-, CN^-, $RCOO^-$, F^-) • Lone-pair containing species (e.g. H_2O, NH_3, CO) • Electron rich π-system (e.g. benzene, pyridine)

In case of CO_2, the bond electron density of CO_2 is more polarized toward the oxygen atoms in the molecule, leaving a partial positive charge on the carbon atom and negative charges on the oxygen atoms. This makes the carbon atom an electron acceptor in a Lewis acid-Lewis base interaction (Kasturirangan, 2007). The interaction of CO_2 with hydroxyl groups has been examined by FTIR spectroscopy that it occurs by CO_2 bonding to only oxygen atoms of the hydroxyl groups. The proposed structure of the CO_2 with the hydroxyl group is described in Figure 15. This specific interaction is thus form by Lewis acid–base or electron donor–acceptor interaction. The formation of electron donor-acceptor complexes between hydroxyl groups and CO_2 molecules is energetically more favorable than a hydrogen-bonded configuration.

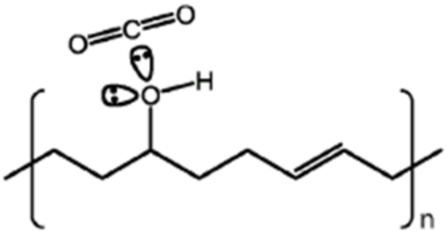

Figure 15. Proposed intermolecular interaction between hydroxyl group (left)/carbonyl group (right) and CO_2 (Gabrienko et al., 2016).

Kim and Kim (2008) have studied CO_2-methylacetate (MA) complexes and the three structures of these complexes; MA-A, MA-B, and MA-C, are shown in Figure 16. The different configurations depend on the location of CO_2 bound to MA. In these three structures, CO_2 is able to bind to the carbonyl oxygen by Lewis acid-Lewis base interaction and bind to α- and/or methoxy protons by C-H●●●O weak H-bonds.

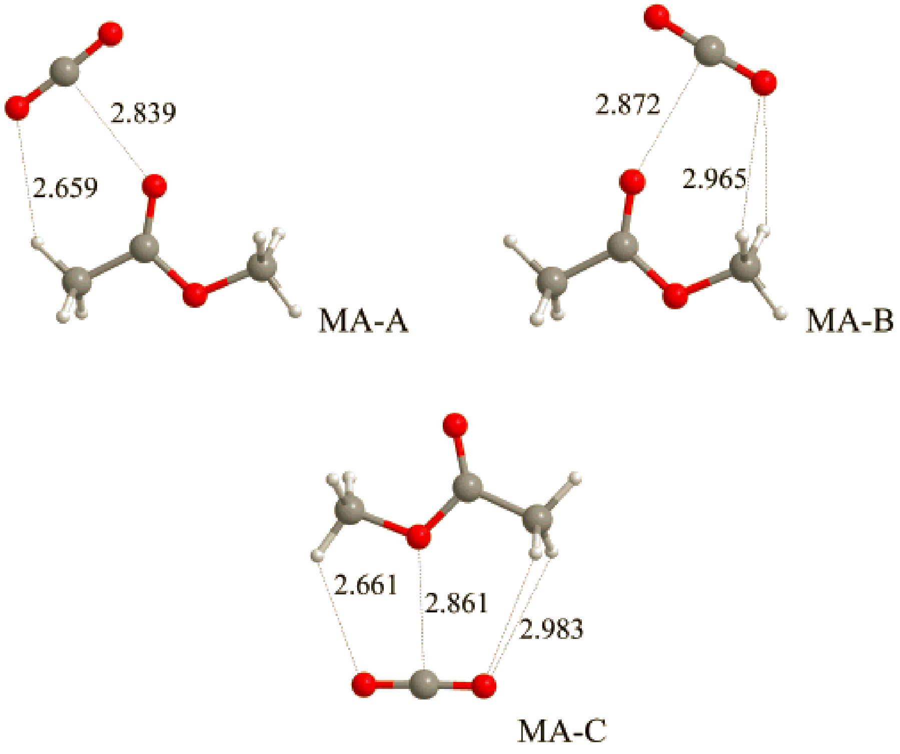

Figure 16. CO_2-methylacetate complexes (lengths are in A°).

1.5 Problem Statement

The main purpose of this work was to fabricate membranes from biodegradable materials via normal casting evaporation drying technique for CO_2 adsorption. Due to the fact that the presence of CO_2 causes environmental as well as natural gas process problems, the studies of how to capture CO_2 have been attractive for long time ago. However, to the best of our knowledge there is no publication related to the application of bacterial cellulose from *Nata de coco* as a membrane for CO_2 capture. To achieve the goal we specified the objectives as follows;

Objective I: Preparation of Bacterial Cellulose (BC)-Based Membranes

In order to prepare new biodegradable membranes for CO_2 capturing purpose, bacterial cellulose (BC), silk fibroin, and ZnO nanoparticles were used, by which bacterial cellulose was matrix. The BC-based membranes were fabricated via simple method into flat-thin films covering on Teflon membranes, used as a support, to form asymmetric membranes. To obtain cellulose nanocrystals and nano-silk fibroin, acid hydrolysis was applied. When cellulosic fibres are subjected to acid, the glucosidic linkages in the cellulose are broken and the degree of polymerization (DP) decreases (Palme et al., 2016). Also, to fabricate homogeneous films, ultrasonication was utilized for isolating the fibrils (Tsalagkas, 2015).

Objective II: Study of CO_2 Interaction with BC-Based Membranes

CO_2 adsorption study was the main objective in this work. We investigated the active membranes by determining the changes of CO_2 IR absorption spectra after interaction of CO_2 in variation of exposure time through the ATR-FTIR spectroscopy instrument. The results obtained from the FTIR spectra provided both qualitative and quantitative analysis. The active sites within the membrane, including, OH groups, CONH groups, and ZnO surfaces, were expected to be favorable of CO_2 attachment.

CHAPTER II

MATERIALS AND METHODS

2.1 Materials

Nata de coco, as a source of bacterial cellulose (BC), was supplied by Thongaumphai's production, Thailand. Silk cocoon from silk worm *Bombyx Mori* was obtained from Chul Thai Silk Co., Ltd., Thailand. Sodium hydroxide (NaOH), sodium carbonate (Na_2CO_3), zinc oxide (ZnO) powder (10-30 nm in size), and 37% hydrochloric acid fuming solution (HCl) were purchased from Sigma-Aldrich Co., Hungary. High purity 99.95%carbon dioxide (CO_2) were obtained from MESSER, Hungary. All chemicals were used as received without further purification. Teflon membranes (Porafil®); pore size 0.45 mm, diameter 47 mm, used as a support, were supplied by Macherey-Nagel.

2.2 Experimental details

2.2.1 Purification of Raw Nata de coco and Preparation of Dried Bacterial Cellulose Films

Nata de coco was firstly cut and soaked in water for almost 1 week and then cut again into small pieces and boiled in distilled water until pH~7. To further improve the purity (remove non-cellulosic materials), *Nata de coco* was treated in 0.01M NaOH solution at 80°C under continuous stirring. After the alkaline treatment, the color of *Nata de coco* changed from pale yellow into white and, eventually, transparent gel was formed. The clear gel was subsequently heated in distilled water several times under continuous stirring until the pH became neutral. Finally, the purified *Nata de coco* was blended by a laboratory blender and dried into silicone trays in an oven to obtain dried bacterial cellulose films. The dried films (Figure 17) were further used for preparation of microfibrillated and nanocrystalline cellulose suspensions.

Figure 17. Dried bacterial cellulose (BC) films in a silicone tray.

2.2.2 Preparation of Microfibrillated Bacterial Cellulose Suspension

In order to prepare microfibrillated bacterial cellulose suspension, the 0.1 %w/v of the dried bacterial cellulose films were cut into small pieces and immersed in 80 ml distilled water. Then, sonication was applied at frequency of 20 kHz with a maximum power 20 W/cm^2 using an 18 mm tip diameter of horn (Tesla 150 WS) until a well dispersed colloid solution was obtained. Sonication is useful for isolation of cellulose fibrils and fabrication homogeneous films (Tsalagkas, 2015).

2.2.3 Preparation of Nanocrystalline Bacterial Cellulose Suspension

The dried bacterial cellulose films (from the section 2.2.1) were kept in a desiccator with a 37% HCl fuming solution. During this process, the degradation of cellulose occurred (Khan, 2014) and the nanocrystalline bacterial cellulose was obtained. After hydrolysis by HCl, nanocrystalline BC was immersed in 80 ml distilled water (0.1%w/v) and sonicated in the same way as the microfibrillated BC.

2.2.4 Preparation of ZnO Nanoparticles Suspension

0.008g (0.01%w/v) of ZnO nano-powder (10-30 nm in size) was dissolved in 80 ml distilled water and sonicated until a well disperse of ZnO nanoparticles suspension was obtained.

2.2.5. Purification of Silk Cocoon (Degumming) and Preparation of Nano-Silk Fibroin Suspension

Figure 18. Silk cocoons from silk worm *Bombyx Mori*.

Silk fibroin was obtained by reeling from the silk cocoon (Yang et al., 2000; Jung and Jin, 2007; Mitropoulos et al., 2015). Figure 18 shows an image of silk cocoons from silk worm *Bombyx Mori*. To remove gum or sericin, the cocoons were boiled in 0.02 M Na_2CO_3 for 30 min and washed in water at 50 °C. This process was repeated several times. The degummed silk fibroin was then dried in an oven at 70 °C (Sah and Pramanik, 2010). The dried silk fibroin was placed in a desiccator under the 37% HCl fuming condition for hydrolysis process similar to the preparation of nanocrystalline BC. In the acid system, fibroin chains are gradually degraded with time because of acid hydrolysis (Ming et al., 2014). In order to prepare nano-silk fibroin suspension, the hydrolyzed silk fibroin (0.1%w/v) was immersed into 80 ml distilled water and sonicated.

2.2.6 Fabrication of Bacterial Cellulose-Based Membranes by Evaporation Casting

The basic BC membrane was prepared by mixing microfibrillated bacterial cellulose suspension, and nanocrystalline bacterial cellulose suspension. 50%v/v (or ~4.8%w/w) ZnO nanoparticles suspension and 10%v/v (or ~10%w/w) nano-silk fibroin suspension were added into that mixture to prepare the ZnO- and silk fibroin-modified BC membranes, respectively. Each mixture suspension (30 ml) was poured onto a Teflon membrane (used as a support) and dried by normal evaporation casting in an oven. Three types of the bacterial cellulose-based membranes on Teflon supports were obtained:

- Basic BC membrane
- BC membrane with nano-silk fibroin
- BC membrane with ZnO nanoparticles.

The overall steps of BC-based membranes preparation is demonstrated in Figure 19.

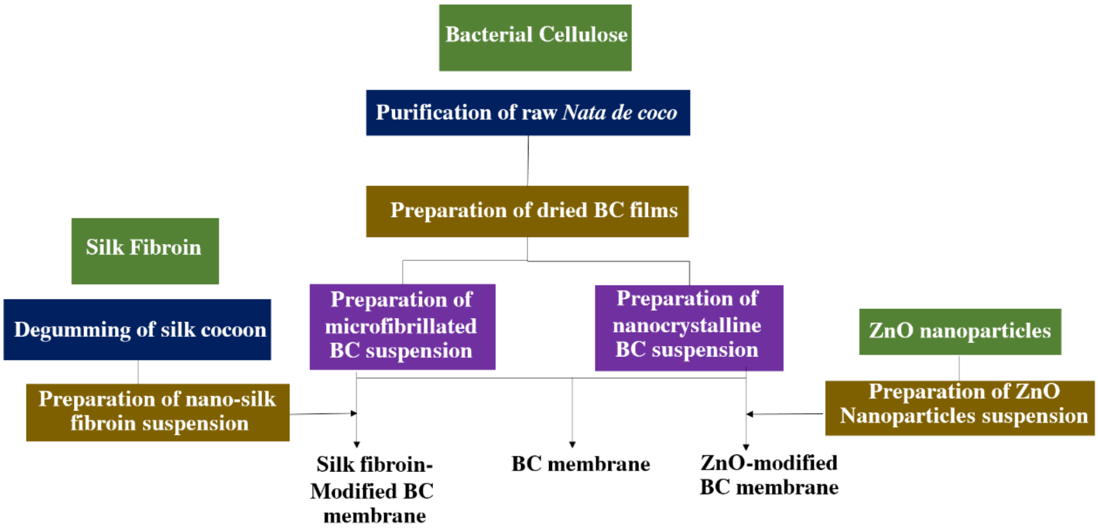

Figure 19. Flow process diagram of BC-based membranes preparation.

2.2.7 ATR (Attenuated Total Reflection)-FTIR Spectroscopy Studies of the Interaction with CO_2

IR spectra were recorded with a Jasco FT/IR6300 equipped with an ATR PRO 470-H spectrometer. In order to obtain control spectra, the BC-based membranes were heated above 100°C to remove some sorbed CO_2 from normal atmosphere, following by recording the ATR-FTIR spectroscopy as the control spectra. For determining the changes of CO_2 spectra after CO_2 adsorption, the samples were measured again after keeping the membranes in a tighten reactor under CO_2 3 bars for 8h, 16h, and 24h. The pressurization process is schematically shown in Figure 20. The spectra were collected by using air as a background. A total of 30 accumulative scans were taken per sample with a resolution of 4 cm^{-1}, in the frequency range of 4000-400 cm^{-1}, in the absorbance mode. The experiment was done at room temperature, replicated three times. The spectra were analyzed and calculated integrated absorption bands via OriginPro 8 software (OriginLab Corporation) and resolved into particular peaks using PeakFit (v4.12) software.

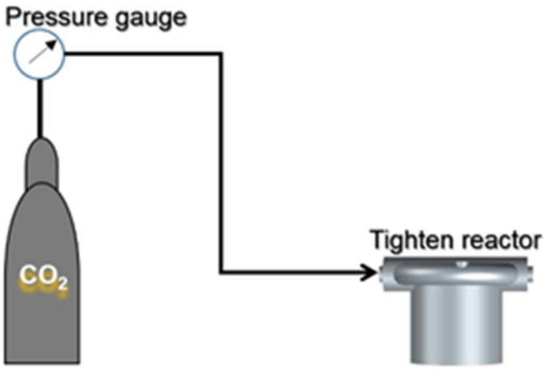

Figure 20. Schematic representation of the pressurization process.

2.3 Characterization of the BC-Based Membranes

2.3.1 Structual Analysis of BC-Based Membranes by ATR (Attenuated Total Reflection)-FTIR Spectroscopy

Infrared spectra of BC-based membranes were characterized by a Jasco FT/IR6300 equipped with an ATR PRO 470-H spectrometer. The spectra were collected over the range of of 4000-400 cm^{-1} with an accumulation of 30 scans, resolution of 4 cm^{-1}, in the absorbance mode.

2.3.2 Morphological Analysis of BC-Based Membranes by FESEM Microscopy

The morphologies of the samples were studied using TESCAN MAIA3 UHR FE-SEM by Beam Deceleration Mode at 500 V and 1.0 kV, and In-Beam SE detector at 2.0 kV for ultra-high resolution and maximum surface sensitivity. Prior to analysis, the samples were coated with a thin layer (5 nm) of Pt.

CHAPTER III

RESULTS AND DISCUSSION

3.1 Structural Analysis of BC-Based Membranes by ATR (Attenuated Total Reflection)-FTIR Spectroscopy

FT-IR spectroscopy measurements were performed to investigate the conformational characteristics of the membranes. Figure 21 presents a general view of FTIR spectra of BC-based membranes in the range of 4000-400 cm^{-1}.

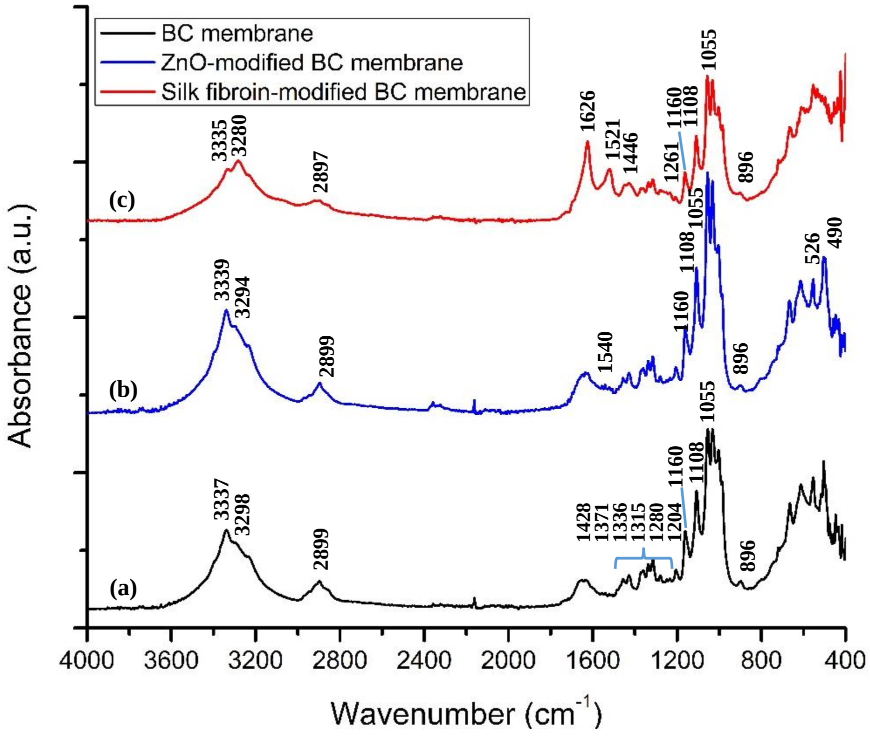

Figure 21. FTIR spectra in the 4000-400 cm^{-1} region of; (a) BC membrane, (b) ZnO-modified BC membrane, and (c) silk fibroin-modified BC membrane.

All spectra of BC-based membranes in Figure 21 exihibits similar vibrational bands of cellulose characteristics, including bands in the 400-700 cm^{-1} region as the OH bending vibrational characteristics, band at 896 cm^{-1} as β-glucosidic linkages between the glucose units (Oliveira et al., 2015), at 1055 cm^{-1} as C-O stretching vibration, at 1108 cm^{-1} as nonsymmetric in-phase ring vibration (Tsalagkas, 2015), at 1160 cm^{-1} as

C-O-C asymmetric stretching vibration, at 1204 cm^{-1} as C-O-C symmetric stretching or OH in plane deformation (Fan et al., 2012), at 1280 cm^{-1} as O-H in-plane bending (Tsalagkas, 2015), at 1315 cm^{-1} as CH_2 rocking vibration at C6 (Fan et al., 2012), at 1336 cm^{-1} as OH in plane bending, at 1371 cm^{-1} as CH bending, at 1428 cm^{-1} as CH_2 bending, at around 1640 cm^{-1} as OH bending of absorbed water, at ~2899 cm^{-1} as CH stretching vibration, and broad band at ~3280 and ~3340 cm^{-1} as OH stretching vibration; inter and intra H-bond respectively (Tsalagkas, 2015). To identify any changes of spectral bands occur after modification with ZnO nanoparticles and silk fibroin, Figure 21(b) and 21(c) are demonstrated. The spectrum obtained for ZnO-modified BC membrane in Figure 21(b) presents the characteristics of cellulose bands as similar positions to the pristine BC membrane spectrum together with the bands at 490 cm^{-1} and 526 cm^{-1} assigned to the ZnO stretching modes, and broad bands around 1540 cm^{-1} corresponding to Zn-OH bending mode (Xiong et al., 2006; Martinez et al., 2011; Djaja et al., 2013).

The obtained spectrum related to the introduction of silk fibroin to BC matrix displays in Figure 21(c), it also shows characteristics vibrational bands of cellulose as well as characteristics of silk fibroin. Due to the presence of amide groups in silk fibroin, the presented bands at 1626 cm^{-1}, 1521 cm^{-1}, 1446 cm^{-1} and 1261 cm^{-1} attributed to the absorption peak of the peptide backbone of amide I (C =O stretching), amide II (N-H bending), and amide (III) (C-N stretching), respectively. The bands at 1626 cm^{-1}, 1521 cm^{-1} and 1261 cm^{-1} are indicative of crystalline β-sheet molecular conformation (silk II) of silk fibroin absorption peaks while we could not find the characteristics of random coil conformation and α-helix (silk I) absorption peaks (Zhang et al., 2012). The strong intensity of the β-sheet bands proves the presence of crystallinity of silk fibroin.

Yang et al. (2000) found that the peak at 1658 cm^{-1} of the random coil conformation disappeared for blend membranes (silk fibroin/cellulose) and presented the β-form absorption band at 1628 cm^{-1}. They suggested that the random coil conformation of silk fibroin can be converted into β-sheet conformation by blending with cellulose owing to the formation of intermolecular H-bonds between cellulose and silk fibroin.

As the addition of silk fibroin into the cellulose results in increasing number of intermolecular hydrogen bonds, the wide absorption bands at 3337 cm^{-1} responsible for the O-H stretching vibration (intra H-bonding) of BC membrane in Figure 21(a) shows the peak shifted to a lower wavenumber (3335 cm^{-1}) in Figure 21(c) resembling to

(Wang et al., 2016) and simultaneously decrease in the intensity of this peak. Furthermore, the prominent peak at 3280 cm^{-1} was observed from the silk fibroin-modified BC membrane spectrum (Figure 21(c)), which is corresponded to the vibration of inter H-bonding (Fan et al., 2012). This was the results of an enhancement of the intermolecular H-bonds between OH groups of cellulose and NH in the amide groups of silk fibroin, on the other hand, a decrease in intramolecular H-bonds of cellulose (Yang et al., 2000).

Consequently, there are no important bands changed and no new covalent bonds after ZnO nanoparticles and silk fibroin impregnation into the BC matrix.

Figure 22(a) and 22(b) show a schematic illustration of the Teflon-supported BC membrane films investigated in this study. BC microfibrils and nanocrystals were used as the active materials for the interaction with CO_2. The BC nanocrystals were introduced into the BC microfibril network in order to obtain the films with nano-sized pores. An attempt was made to increase the affinity of the membrane towards CO_2 by modifying BC membrane with silk fibroin protein and ZnO nanoparticles. The image of the BC membrane prior to modification is shown in Figure 22(c). Macroscopically, the modified BC membranes were very similar to the basic BC membranes.

The BC-based membranes are in the form of thin films on the Teflon supports after normal evaporation casting drying. The thickness of a whole membrane is about 265 µm; BC-based film is around 20 µm, and 5 cm in diameter.

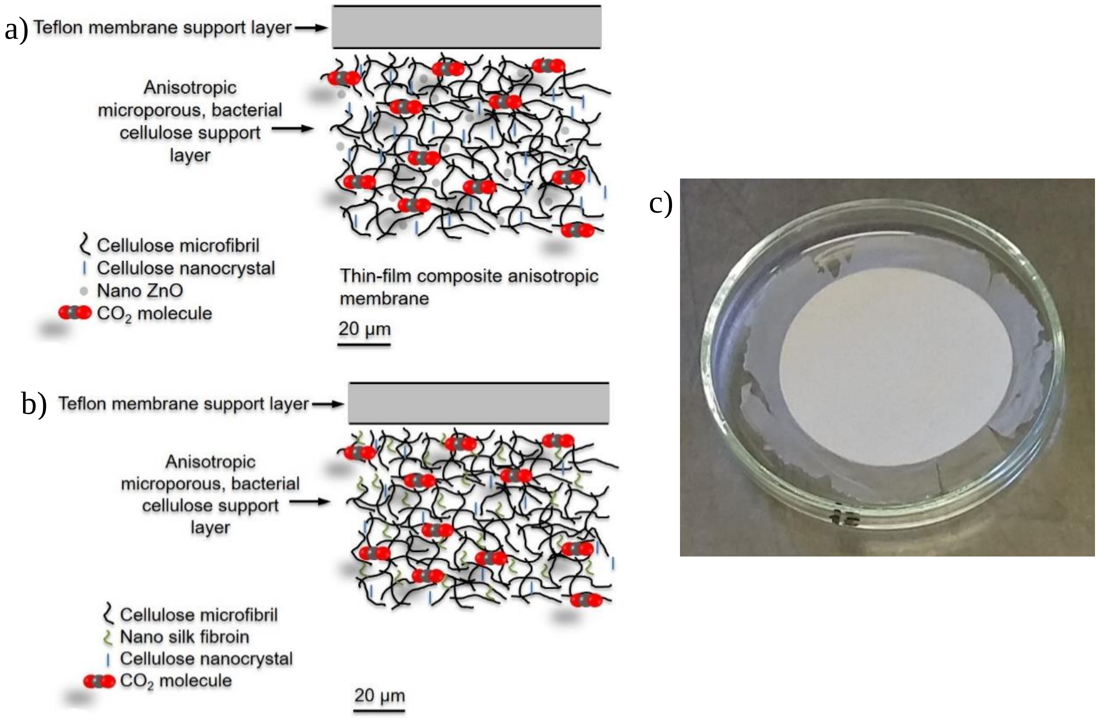

Figure 22. Schematic illustration of the Teflon-supported bacterial cellulose (BC) membrane and its interaction with CO_2. Each membrane contained cellulose microfibrils and nanocrystals. In order to increase their affinity towards CO_2 they were additionally modified with a) silk fibroin protein or b) with ZnO nanoparticles. c) The image of the pure Teflon-supported BC membrane.

3.2 Morphological Analysis by FESEM Microscope

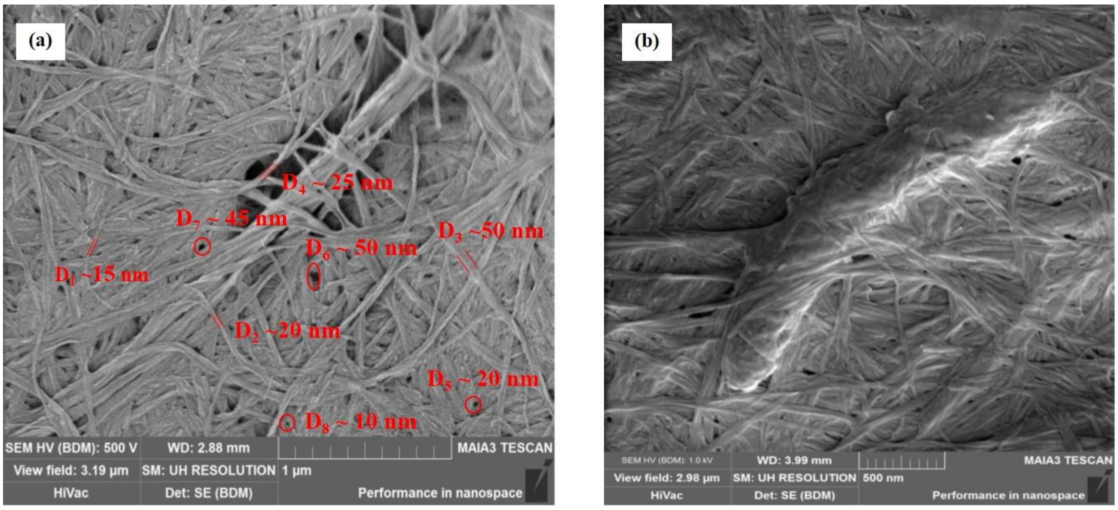

Figure 23. FESEM images of basic BC membrane.

Figure 23(a-b) shows the surface images of basic BC membrane which was performed on a TESCAN MAIA3 FE-SEM at 500V and 1.0 kV, respectively. They exhibit a crisscross mesh structure with randomly entangled nanofibrils of bacterial cellulose. The diameter of cellulose fibrils was in the range from 15 to 50 nm, labeled with red color, and the length was few hundreds of micrometers. This 3D network nanocellulose fibrils also provided the porous structure with the size of around 10-50 nm in diameter.

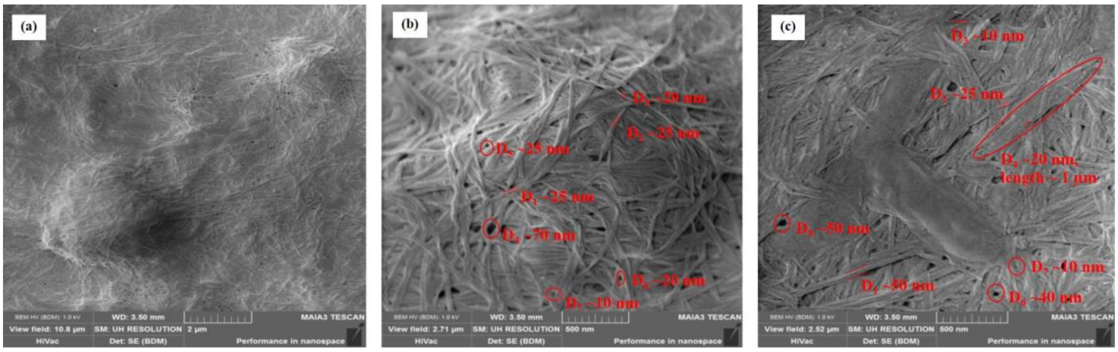

Figure 24. FESEM images of silk fibroin-modified BC membrane.

The addition of silk fibroin into the BC matrix seems to have a similar network structure as well as the same range of cellulose fibrils' size (10-50 nm) as that of the basic BC membrane as presented in Figure 24(a-c). A larger view area in Figure 24(a) illustrates homogenous surface of this modified BC membrane. The presence and distribution of silk fibroin with shorter and sharper fibrils, in comparison with cellulose fibrils, is clearly shown in Figure 24(c). It was also observed the bundles of silk fibroin with the approximate length of 1 µm and 20 nm in diameter of each fibroin fibrils in the BC matrix from Figure 24(c). The rounder and bigger pores (10-70 nm in diameter) were found from this silk fibroin modified BC membrane presumably according to the presence of shorter silk fibrils.

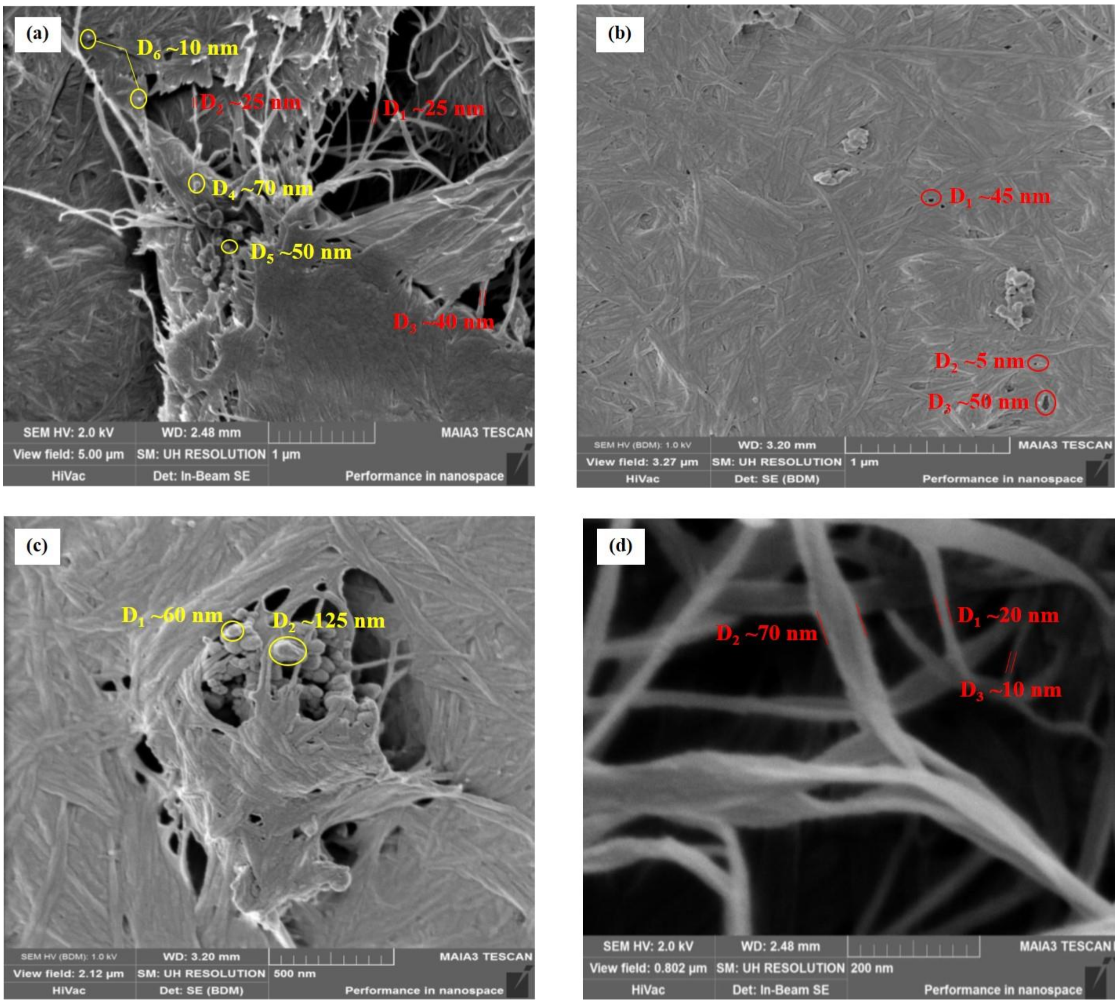

Figure 25. FESEM images of ZnO nanoparticles-modified BC membrane.

In the composite membrane with ZnO nanoparticles, the morphology of fractured surfaces of this membrane is exhibited in Figure 25(a) revealing the presence of ZnO nanoparticles within the BC nanofibrils network. The agglomeration of ZnO nanoparticles was also noticed from Figure 25(a-c), where the size of ZnO nanoparticles were labeled with yellow color. Although, the nanoparticles of ZnO were below the surface of cellulose nanofibrils, CO_2 molecules were able to interact with them via diffusion through the pores (5-50 nm in diameter) of the BC matrix. As can be seen in Figure 25(d), it shows a singular nanocellulose fibril which the size was in the same range as the fibrils in other membranes.

From the surface analysis, these FESEM images confirm that all of the BC-based membranes formed a fine nanofibrils entangled network structure with porous in nano-size. Consequently, these membranes are suitable for using as gas separation membrane owing to the dense structure with distribution of nano-sized pores and the presence of active sites for CO_2. This may be resulted in an enhancement in both permeability and selectivity.

3.3 ATR (Attenuated Total Reflection)-FTIR Spectroscopy Studies of the Interactions with CO_2

Three types of BC-based membranes; BC, silk fibroin-modified BC, and ZnO-modified BC, were subjected to investigate the interaction with CO_2 in this work. These BC-based samples contain particular functional groups that were expected to interact with CO_2. To obtain spectroscopic data for the behavior of CO_2 sorption to the BC-based samples, all of samples were pressurized under CO_2 3 bar for various times (8h,16h,24h) and examined using ATR-FTIR spectroscopy. The interaction of the membrane materials with CO_2 were studied by considering two regions of CO_2 vibrational mode spectra: 740-610 cm^{-1} (bending vibration of CO_2) and 2400-2300 cm^{-1} (asymmetric stretching vibration of CO_2). Prior the analysis, all of the spectra were shifted to have the same intensity absorbance value at a fixed wavenumber where each spectra absorbance intensity shows the closest value.

3.3.1 Bending (υ_2) Vibrational Mode of CO_2

Changes in the bending mode of CO_2 when CO_2 reacts with polymers have been investigated by Kazarian et al. (1996), Nalawade et al. (2006), and Yuan and Teja (2011). The ATR-FTIR absorption spectra of BC-based membrane samples in the 740-610 cm^{-1} region (characteristic for the CO_2 bending absorption band) are shown in Figure 26-28. The FTIR spectra of the control samples in all BC-based membranes, prepared by heating over 100°C, show broad absorption peaks of CO_2 in the bending mode region suggesting the presence of entrapped CO_2 from atmosphere within the membranes that could not be removed entirely. However, their absorbance values (intensity) are noticeable lower than that of the CO_2 pressurized samples. In order to investigate whether prolonged exposure to CO_2 gas will affect the intensity and the position of that peak, the membranes were kept in a tighten reactor under 3 bar for 8, 16 and 24h. The FTIR spectra of these membranes show the remarkable peaks for the sorbed CO_2 in the range of the bending mode region of CO_2. With respect to the spectra of the control samples, the intensity of the CO_2 bending mode peaks (υ_2) significantly increase after the samples exposure of CO_2 as demonstrated in Figure 26-28.

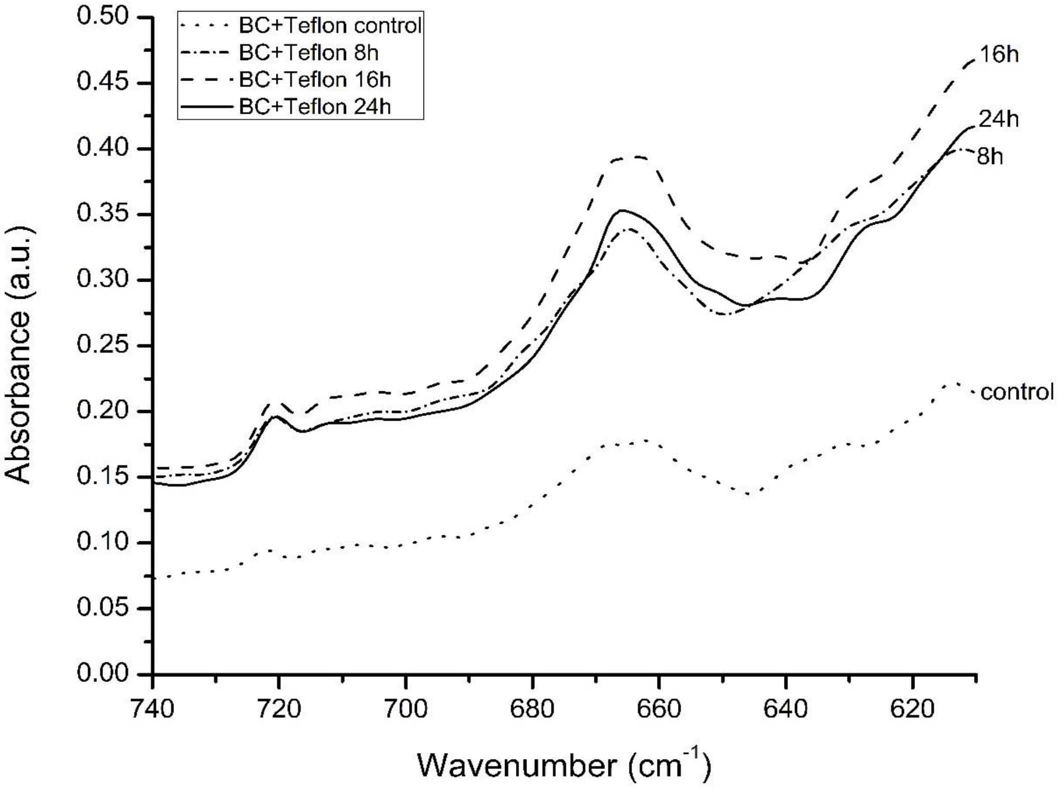

Figure 26. ATR-FTIR spectra of BC membranes in the bending mode region (740-610 cm^{-1}) of CO_2 in all conditions: after heating above 100°C (control) and after pressurizing with CO_2 at 3 bars for 8 h, 16 h and 24 h.

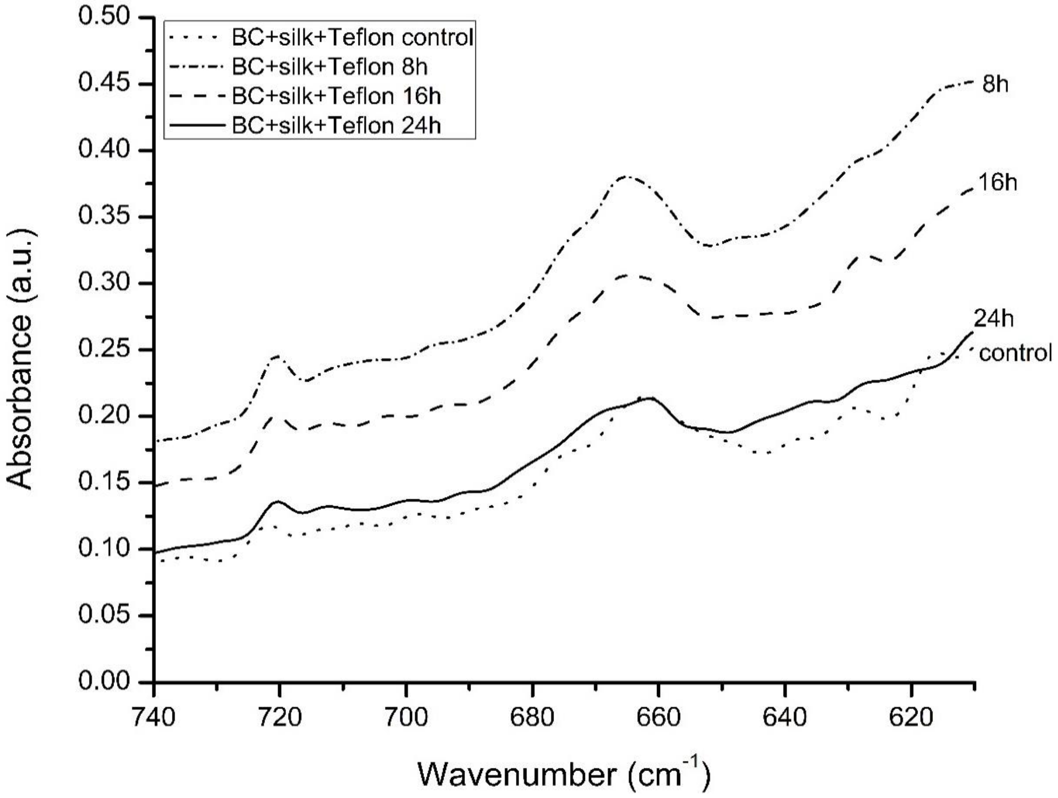

Figure 27. ATR-FTIR spectra of silk fibroin-modified BC membranes in the bending mode region (740-610 cm^{-1}) of CO_2 in all conditions: after heating above 100°C (control) and after pressurizing with CO_2 at 3 bars for 8 h, 16 h and 24 h.

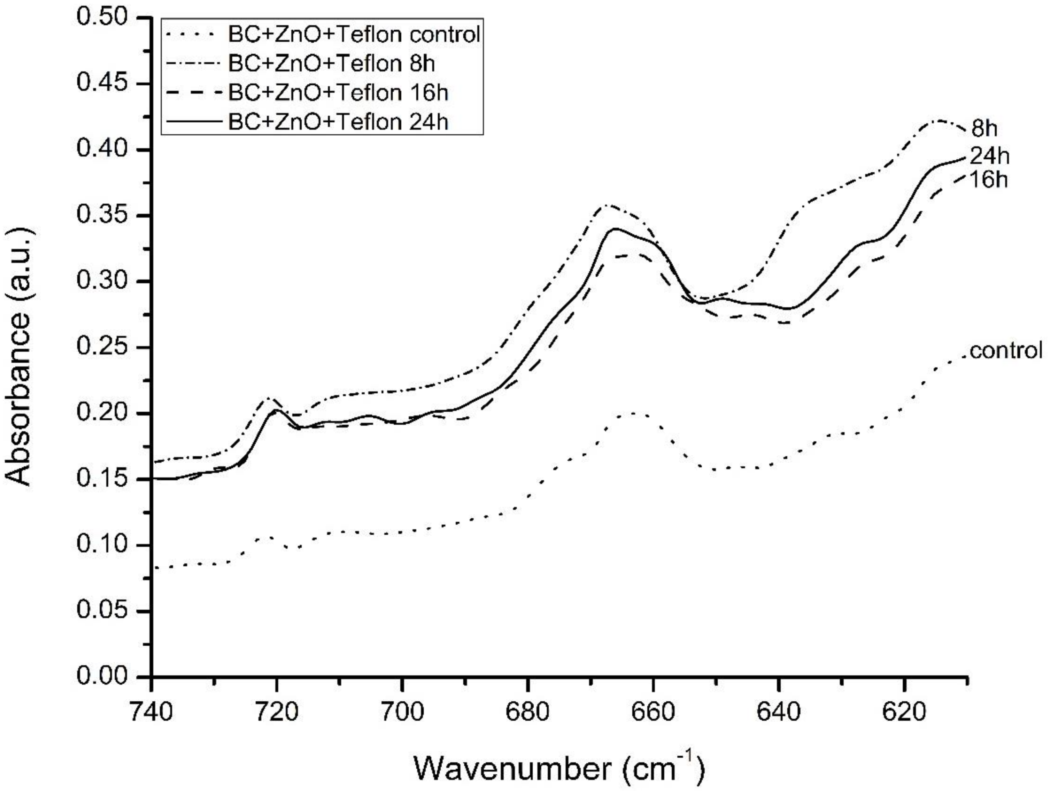

Figure 28. ATR-FTIR spectra of ZnO-modified BC membranes in the bending mode region (740-610 cm^{-1}) of CO_2 in all conditions: after heating above 100°C (control) and after pressurizing with CO_2 at 3 bars for 8 h, 16 h and 24 h.

Figure 26 displays the FTIR spectra of sorbed CO_2 from different exposure times of the pressurized BC membranes and the control BC sample. The absorbance intensity enhances noticeably after subjection to CO_2. The highest intensity and distinguished spectrum of the basic BC sample spectra is the spectrum of the BC sample after 16h introduction of CO_2. Also, Figure 27 as well as Figure 28 show a comparison between the control sample and the CO_2 pressurized sample of silk fibroin- and ZnO-modified BC membranes, respectively. In case of these two types of membranes, the 8h CO_2 pressurized sample appears as the prominent spectrum. As can be observed (Figure 26-28), the shape of the bands corresponding to the CO_2 bending vibrational mode changes after pressurized the membranes with CO_2 indicating possible v_2 band splitting as a result of the interaction with membrane functional groups. Moreover, it was also noticed that the CO_2 absorption spectra bands of silk fibroin- and ZnO-modified BC samples seem broader than that of BC samples. To more clearly examine the difference, we resolved the peak into particular peaks by PeakFit in the CO_2 bending mode region of the control and the most outstanding absorption peak in each type of membrane, the obtained peaks are shown in Figure 29-31.

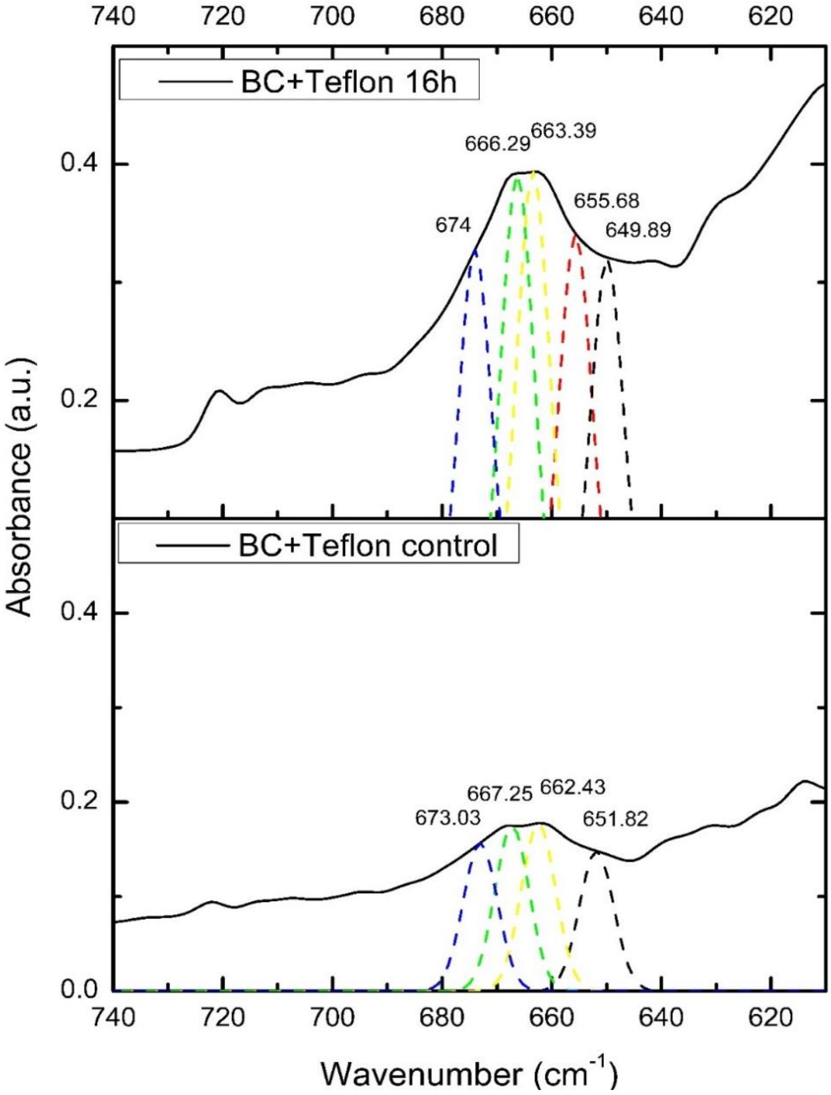

Figure 29. ATR-FTIR spectra of BC membrane; control sample and sample after pressurizing with CO_2 16h, in the bending mode region (740-610 cm^{-1}) of CO_2 after resolved into particular peaks by PeakFit.

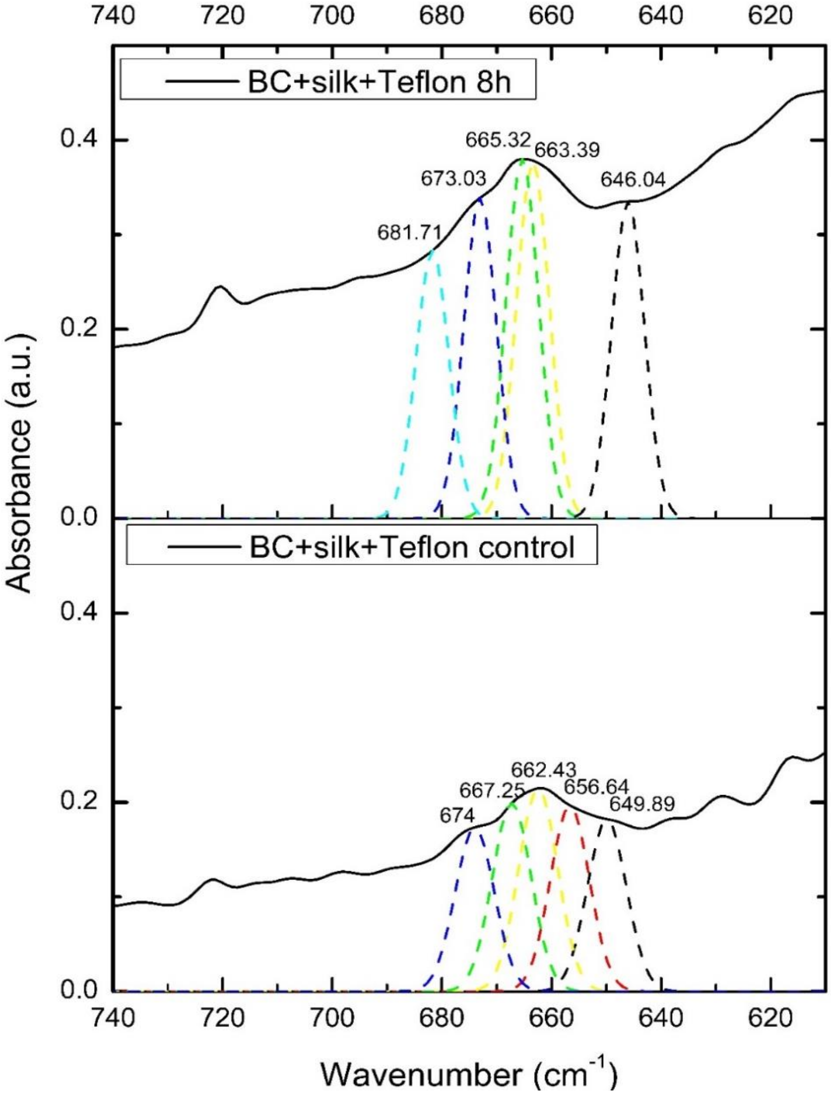

Figure 30. ATR-FTIR spectra of silk fibroin-modified BC membrane; control sample and sample after pressurizing with CO_2 8h, in the bending mode region (740-610 cm^{-1}) of CO_2 after resolved into particular peaks by PeakFit.

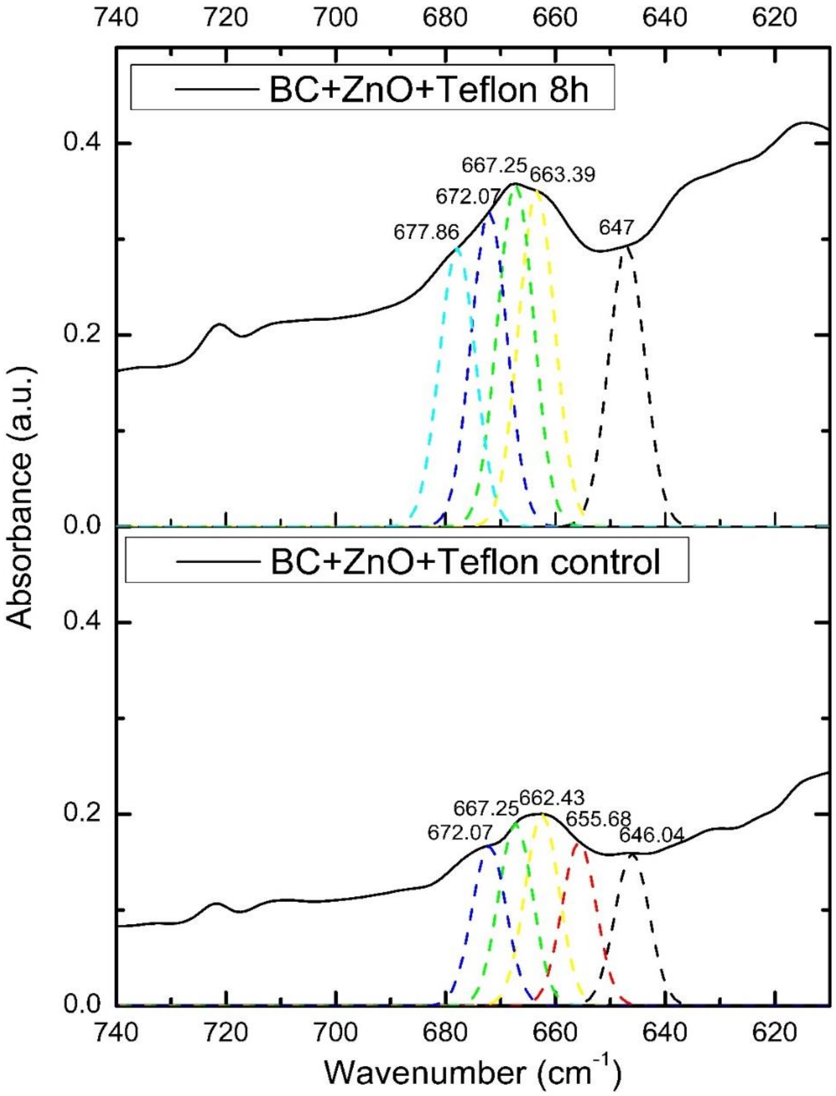

Figure 31. ATR-FTIR spectra of ZnO-modified BC membrane; control sample and sample after pressurizing with CO_2 8h, in the bending mode region (740-610 cm^{-1}) of CO_2 after resolved into particular peaks by PeakFit.

Due to the fact that CO_2 is a weak Lewis acid, thus, it can interact with Lewis base to form an electron donor-acceptor complex, by which carbon atom of the CO_2 acts as an electron acceptor. The consideration of spectral bands of bound CO_2 can be provided the information about the interaction of CO_2 with the functional groups of the polymers (Yuan and Teja, 2011), for example, Kazarian et al. (1996) pointed out that Lewis acid-base interactions of CO_2 and carbonyl groups lead to the formation of a bent T-shaped complex that can be detected by the splitting of the bending mode of CO_2 bands.

Likewise, in our studies, the resolved spectra of each sample (Figure 29-31) are the evidence of the CO_2 trapped in the membrane materials, which under the envelope of the bending mode peak of CO_2 clearly presents the splitting phenomenon. When CO_2 takes part in the formation of an electron donor-acceptor complex, the splitting of the CO_2 bending absorption band occurs (Yuan and Teja, 2011). Figure 29 shows the resolved IR spectra of the basic BC samples; control and 16h condition. Four splitting peaks at 651 cm^{-1}, 662 cm^{-1}, 667 cm^{-1}, and 673 cm^{-1} can be seen in the BC control spectrum, while, five peaks at 649 cm^{-1}, 655 cm^{-1}, 663 cm^{-1}, 666 cm^{-1}, 674 cm^{-1} are of the 16h CO_2 pressurized BC sample spectrum. Table 3 summarizes the vibrational band positions in the bending region of sorbed CO_2 from the deconvoluted BC-based membrane spectra. As can be seen in Figure 29, the resolved spectrum of the BC membrane pressurized with CO_2 16h do show an additional band at ~655 cm^{-1} that it is not observed in the spectrum of the control membrane. Also, the peak at 651 cm^{-1} of the control sample shifted to lower frequency at 649 cm^{-1} after 16h CO_2 pressurization. The prominent peaks of the resolved spectra are near 663 and 667 cm^{-1}. Similar results were reported by Kazarian et al. (1996) for the poly(methyl methacrylate) (PMMA) film pressurized with CO_2. They have noticed that the interaction of CO_2 with carbonyl group of PMMA induces change in the v_2 peak shape and appearance of the shoulder at the lower frequencies. After envelope of the shifting band was resolved into particular peaks, they found that new absorption bands positioned at 662 and 654 cm^{-1}.

Table 3. Carbon dioxide bending vibrational band positions from the deconvoluted BC-based membrane spectra.

Membranes	**Splitting lines in the CO_2 bending region (cm^{-1})**
BC+Teflon	
• Control	651.82, 662.43, 667.25, 673.03
• 16h CO_2 pressurized	649.89, 655.68, 663.39, 666.29, 674
BC+Silk+Teflon	
• Control	649.89, 656.64, 662.43, 667.25, 674
• 8h CO_2 pressurized	646.04, 663.39, 665.32, 673.03, 681.71
BC+ZnO+Teflon	
• Control	646.04, 655.68, 662.43, 667.25, 672.07
• 8h CO_2 pressurized	647, 663.39, 667.25, 672.07, 677.86

The deconvoluted absorption spectra of the silk fibroin-modified samples; control and 8h condition, are shown in Figure 30, where five different splitting peaks are found in both conditions. The control spectrum presents (Table 3) the peaks at 649 cm^{-1}, 656 cm^{-1}, 662 cm^{-1}, 667 cm^{-1}, and 674 cm^{-1}, while, the 8h CO_2 pressurized sample spectrum reveals the peaks at 646 cm^{-1}, 663 cm^{-1}, 665 cm^{-1}, 673 cm^{-1}, and 681 cm^{-1}. The disappeared peak at ~655 cm^{-1} presumably due to the result of the overlapping with the peak at ~663 cm^{-1}. However, there is an extra peak at 681 cm^{-1} for the 8h CO_2 pressurized sample. The absorption band at 649 cm^{-1} of the control also shifted to 646 cm^{-1} for the pressurized sample. The bands ~663 and ~665 cm^{-1} are the main peaks of the CO_2 pressurized silk fibroin- modified BC membrane (Figure 30).

Similarly, the resolved ZnO-modified BC sample spectra; control and 8h CO_2 pressurized condition, also reveal five splitting peaks in both conditions as can be seen in Figure 31. The control envelope contains the following peaks (Table 3) at 646 cm^{-1}, 655 cm^{-1}, 662 cm^{-1}, 667 cm^{-1}, and 672 cm^{-1}, concurrently, the peaks at 647 cm^{-1}, 663 cm^{-1}, 667 cm^{-1}, 672 cm^{-1}, and 677 cm^{-1} are of the 8h CO_2 pressurized spectrum. The 677 cm^{-1} line is found as an additional line obtaining from the spectrum of the ZnO-modified BC after pressurization. The main peaks obtained from the envelopes are also around 663 cm^{-1} and 667 cm^{-1} (Figure 31). The appearance of the additional band can be supposed that because of the interaction of CO_2 molecules with the membrane in a specific way, i.e., the formation of intermolecular complexes between CO_2 and functional groups (Gabrienko et al., 2016). Gabrienko et al. (2016) revealed that there are two splitting bands (~660 cm^{-1} and ~650 cm^{-1}) in the bending mode of CO_2 after spectral subtraction, which correspond to CO_2 interacting with the functional groups of the polymers, on the other hand, the bands of physically sorbed CO_2 (657 cm^{-1}) was removed. They claimed that the splitting bands of the bending mode of CO_2 are the main difference between the spectra of physically sorbed CO_2 and CO_2 interacting with the functional groups of the polymers. CO_2 physically sorbed by the polymers do not have any specific interaction between themselves that can be referred as CO_2 dissolved in polymer matrix resulting in swelling of the polymers.

The splitting of the bending mode of CO_2 is related with its arrangement in the complex. Thence, the significant shifts of the in-plane mode and out-of-plane mode toward lower wavenumbers and higher wavenumbers, respectively, can be found due to the perturbation of the electron donor-acceptor interactions (Danten et al., 2005).

The order of the CO_2 bending vibrational frequencies is υ (in-plane bending of associated CO_2) < υ (free CO_2) < υ (out-of-plane bending of associated CO_2) (Yuan and Teja, 2011). As we know, the wavenumber is inversely proportional to wavelength whereas it is directly proportional to the frequency and energy, hence, this frequency order is the same as to the order of wavenumber (“Infrared Spectroscopy”). Additionally, it is noteworthy that the band at ~667 cm^{-1} is assigned to the gas phase of CO_2 arising from free and unassociated CO_2 (Kazarian et al., 1996; Nalawade et al., 2006; Yuan and Teja, 2011). Nalawade et al. (2006) also mentioned that the bands at ~660 cm^{-1} and ~650 cm^{-1} are of the out-of-plane bending and in-plane bending modes of CO_2, respectively. The attachment of CO_2 with a functional group leads to generate two different bending modes of CO_2 which are out-of-plane (higher frequency) and in-plane (lower frequency) modes (Jamróz et al., 1995; Gabrienko et al., 2016).

In regard to the modes assignment from other studies, our resolved peak positions in each IR spectrum could be assigned for the peaks at ~667 cm^{-1}, ~662 cm^{-1}, ~655 cm-

^{1}, and ~650 cm^{-1} as gas phase of CO_2, out-of-plane bending of associated CO_2, physically sorbed CO_2, and in-plane bending of associated CO_2, respectively. It is worthily to note that there are also two arrangements; parallel and perpendicular geometries to the active functional group, for the O-donors of CO_2 molecule in an electron donor-acceptor complex in both out-of-plane and in-plane modes (Jamróz et al., 1995), therefore, the possibility of more pronounced spectral lines associated with these structures can be introduced. According to the spectra (Figure 29-31), we suggested that the split line at ~673 cm^{-1} of all spectra is probably due to this reason. Furthermore, the additional line at 681 cm^{-1} of the silk fibroin-modified sample spectrum as well as at 677 cm^{-1} of the ZnO-modified sample spectrum can be seen obviously after pressurization. This means there might be more specific structures formed between CO_2 and these membrane samples similar to Danten et al. (2005). They cited that more spliting curves referred to more existence interactions resulting in more specific structures. Hence, it can be supposed that the functional groups in the silk fibroin and also the active surfaces of ZnO nanoparticles could improve the specific sites to interact with CO_2 and then form more complexe species compared to the basic BC sample. The possible mechanisms will be further discussed in Figure 38.

The CO_2 interaction with hydroxyl group has been described that CO_2 bonds to only oxygen atom of hydroxyl group to form the CO_2–hydroxyl group complex by the formation of Lewis acid–base or electron donor–acceptor complex owing to the available lone pair of electrons of oxygen atom in hydroxyl group as an electron-donor site (Gabrienko et al., 2016).

From our FTIR results of the CO_2 bending region, the spectra show similar splitting peaks corresponding to CO_2 attached to the functional groups of the BC-based membranes indicates the similarity of formed complexes between CO_2 molecules and the functional groups (Gabrienko et al., 2016). Additionally, the increase of the absorbance of CO_2 bending envelope after pressurization together with the appearance of extra bands, are an evidence of CO_2 sorption to the samples.

Besides, vibration in the antisymmetric stretching υ_3 mode of CO_2 can be also used to determine the interaction of CO_2 with the membranes.

3.3.2 Asymmetric Stretching (υ_3) Vibrational Mode of CO_2

The ATR-FTIR spectra in the asymmetric stretching region (2400-2300 cm^{-1}) of CO_2 show the presence of CO_2 sorption by BC-based samples displayed in Figure 32-34. The effect of CO_2 pressurization on the CO_2 spectra was investigated for each sample. The significant changes of the IR spectra in the asymmetric stretching mode region after exposure to CO_2 compared to the control condition can be apparently seen (Figure 32-34).

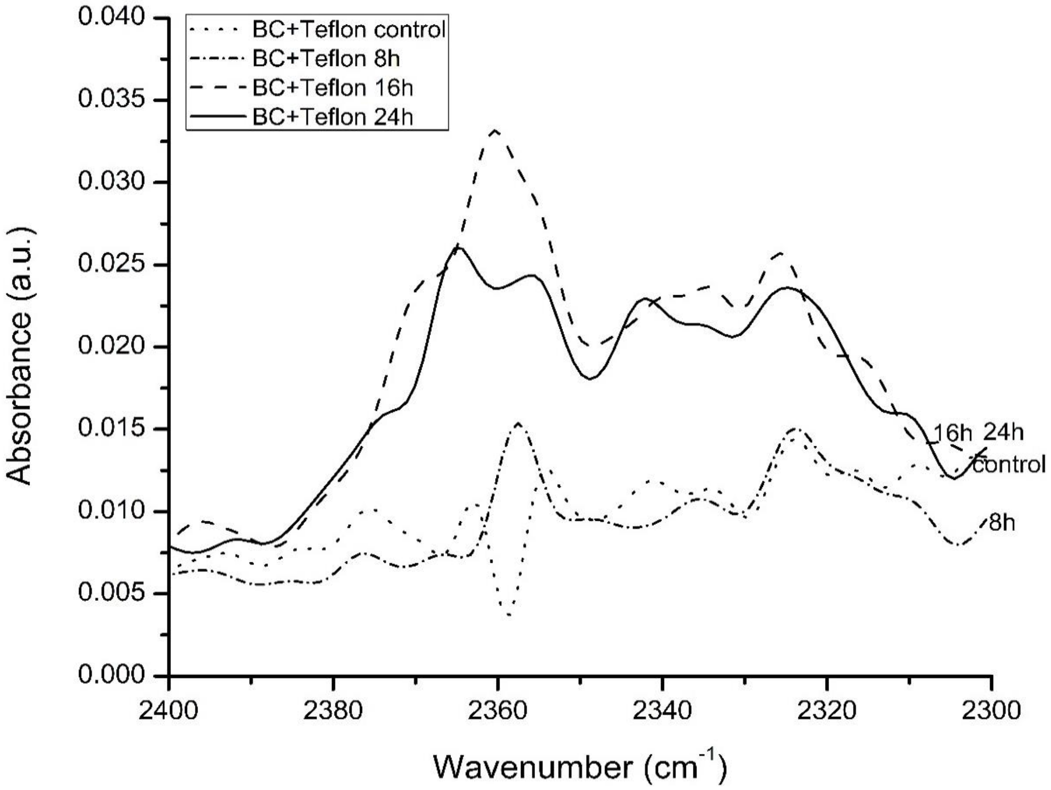

Figure 32. ATR-FTIR spectra of BC membranes in the asymmetric stretching mode region (2400-2300 cm^{-1}) of CO_2 in all conditions: after heating above 100°C (control) and after pressurizing with CO_2 at 3 bars for 8 h, 16 h and 24 h.

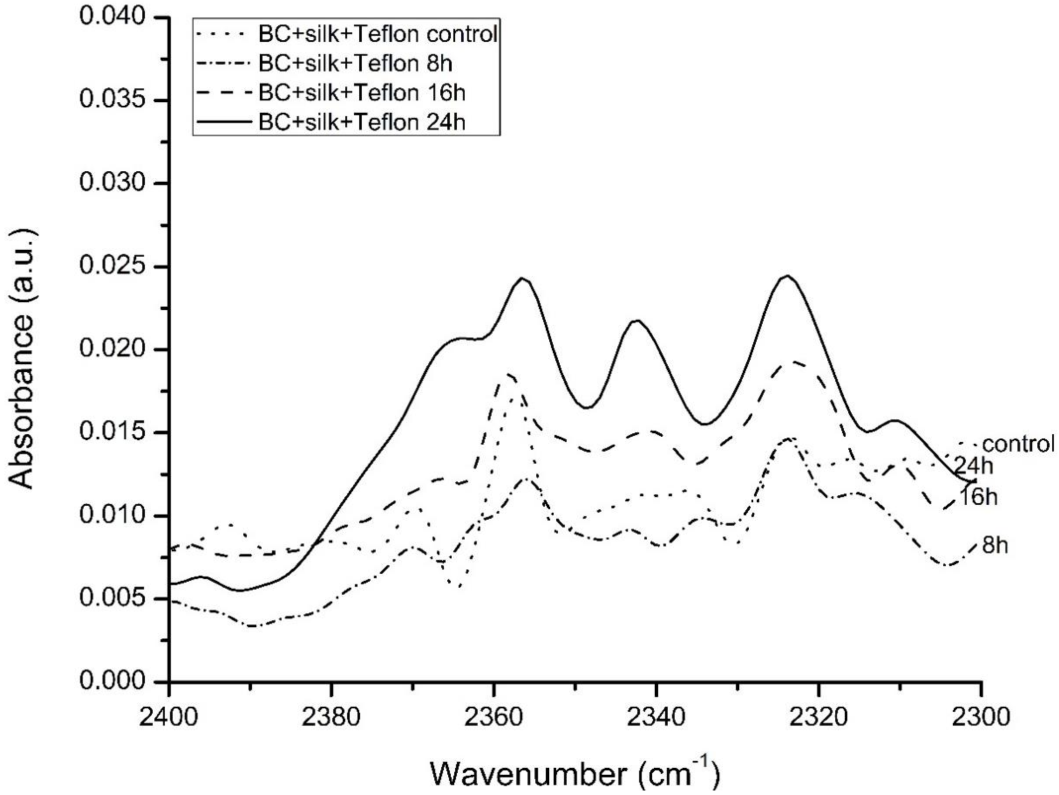

Figure 33. ATR-FTIR spectra of silk fibroin-modified BC membranes in the asymmetric stretching mode region (2400-2300 cm^{-1}) of CO_2 in all conditions: after heating above 100°C (control) and after pressurizing with CO_2 at 3 bars for 8 h, 16 h and 24 h.

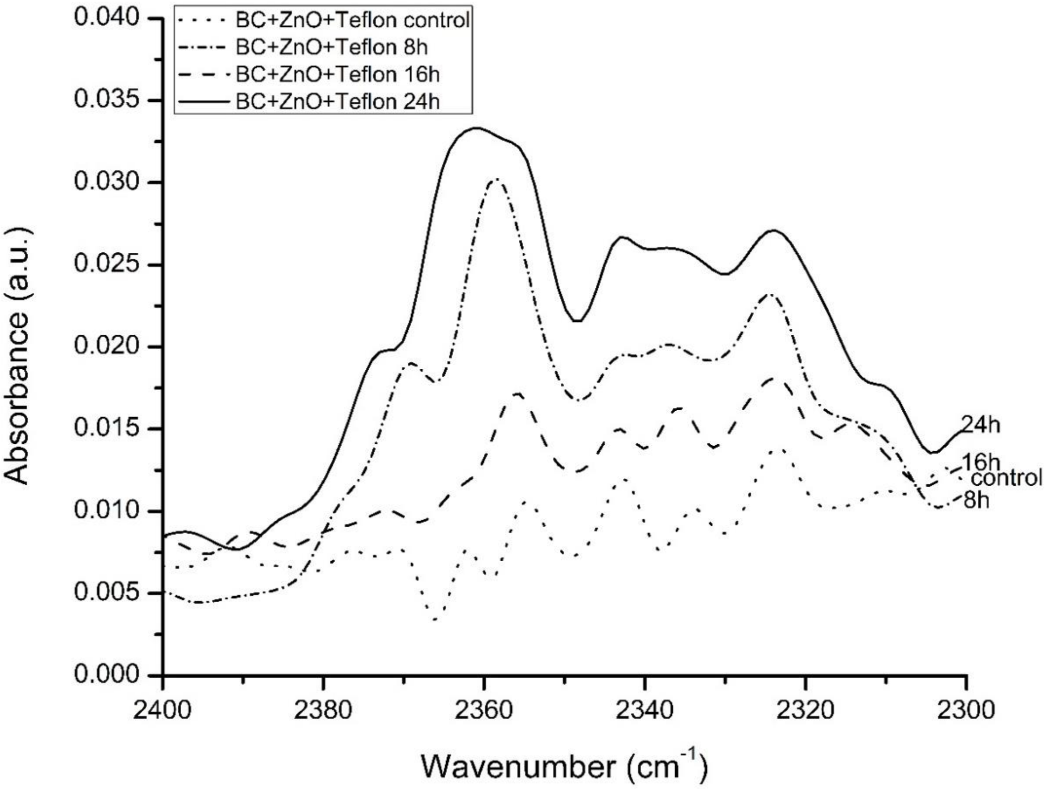

Figure 34. ATR-FTIR spectra of ZnO-modified BC membranes in the asymmetric stretching mode region (2400-2300 cm^{-1}) of CO_2 in all conditions: after heating above 100°C (control) and after pressurizing with CO_2 at 3 bars for 8 h, 16 h and 24 h.

Figure 32 shows a comparison of the spectra in the asymmetric stretching mode region of the basic BC membranes at different exposure times and the basic BC control sample. The corresponding spectra present the peaks which are of the sorbed CO_2. With respect to the BC control spectrum, all of the pressurized sample spectra demonstrate more notable peak in this region, particularly in the case of the 16h CO_2 pressurized sample (Figure 32). This falls in the same trend as the IR result in the bending mode region, which the 16h pressurized sample achieves the most remarkable spectrum. It is then suggested that after prolonging the pressurization time, the bound CO_2-BC complexes vibrate increasingly in both vibrational mode of CO_2. For the silk fibroin-modified BC samples, their IR absorption spectra are revealed in Figure 33. The 24h CO_2 exposure sample spectrum shows the highest intensity of the absorption bands in this region which is opposite to the result from the bending region. This may be presumed that the attached CO_2 with this sample are favorable for the vibration in asymmetric stretching mode after longer duration of CO_2 exposure. In the case of ZnO-modified BC membrane spectra, Figure 34 is illustrated. The prominent spectra can be obtained from the 24h pressurized sample. The control spectrum also provides the lowest intensity and the least outstanding (Figure 34).

Therefore, all of the BC-based membrane spectra (Figure 32-34) show that there are drastic changes in the FTIR spectra in this region after incorporation with CO_2. The IR peak intensity enhancement of the samples after pressurization compared to that of the control sample can be clearly observed from all figures (Figure 32-34). It should be note that an increase in the absorption band intensity reflects the amount of sorbed CO_2 increase. In accordance with changes of spectral curve in the CO_2 asymmetric stretching region, this can support the CO_2-membrane interaction suggestion. Besides, all spectra present several spitting peaks, to clearly notice, we resolved the spectrum in the asymmetric stretching mode region into particular peaks by PeakFit resembles the CO_2 bending mode region for the control and the most remarkable absorption peak in each type of membrane. Peak fitting is often necessary to accurately distinguish the absorption band positions (Baltrusaitis et al., 2011). The obtained peaks are shown in Figure 35-37.

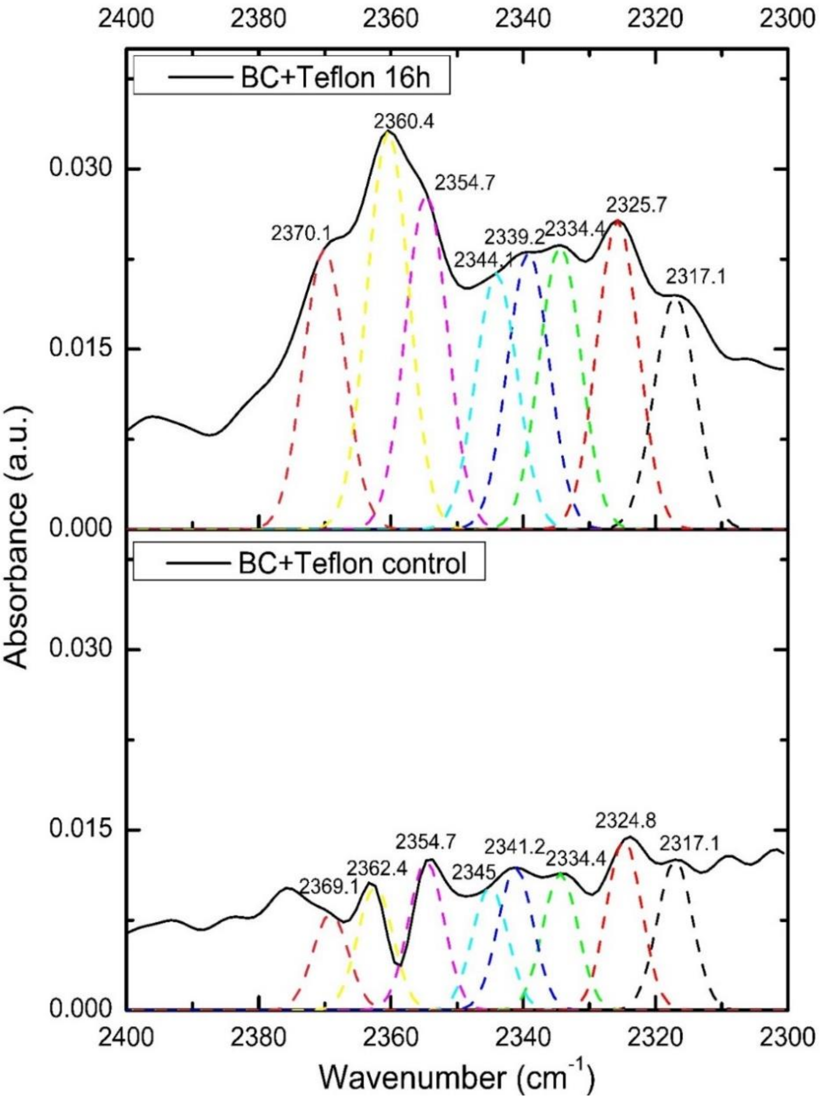

Figure 35. ATR-FTIR spectra of BC membrane; control sample and sample after pressurizing with CO_2 16h, in the asymmetric stretching mode region (2400-2300 cm^{-1}) of CO_2 after resolved into particular peaks by PeakFit.

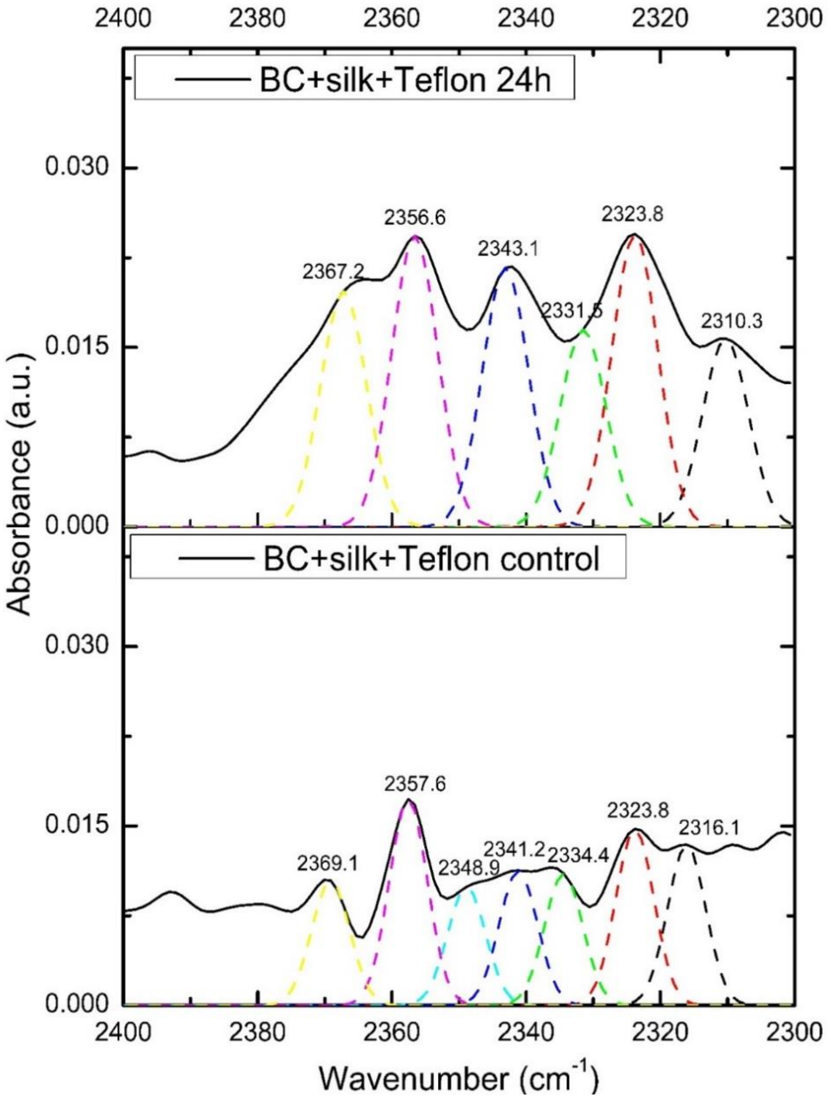

Figure 36. ATR-FTIR spectra of silk fibroin-modified BC membrane; control sample and sample after pressurizing with CO_2 24h, in the asymmetric stretching mode region (2400-2300 cm^{-1}) of CO_2 after resolved into particular peaks by PeakFit.

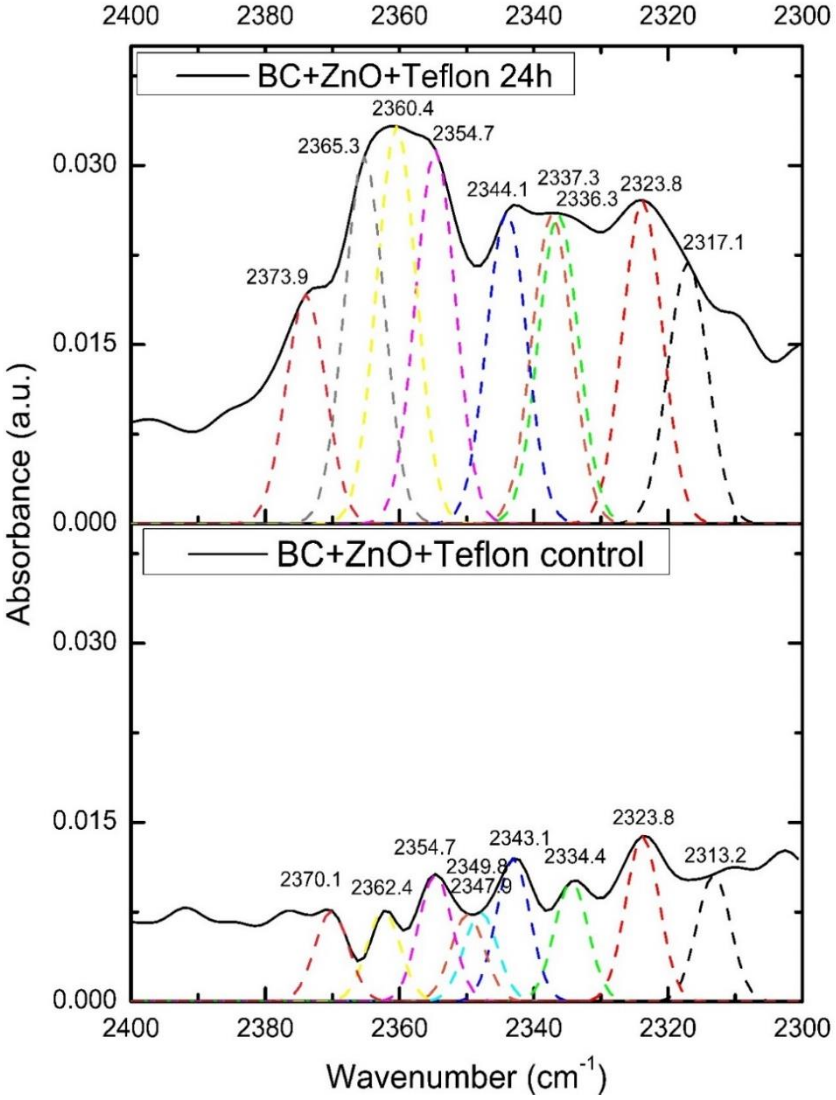

Figure 37. ATR-FTIR spectra of ZnO-modified BC membrane; control sample and sample after pressurizing with CO_2 24h, in the asymmetric stretching mode region (2400-2300 cm^{-1}) of CO_2 after resolved into particular peaks by PeakFit.

Yao et al. (2012) measured the IR absorption spectra of CO_2 absorbed in Mg-MOF74 and Zn-MOF74 and found a main IR absorption band attributed to the asymmetric stretch (υ_3) of CO_2 existed at 2338 cm^{-1} and 2352 cm^{-1} for Zn-MOF74 and Mg-MOF74, respectively, while a shoulder peak at 2325 cm^{-1} for Zn-MOF74 and 2341 cm^{-1} for Mg-MOF74. These peaks are the result of the combination mode (denoted as; $\delta_2 - \delta_1 + \upsilon_3$) of the stretch mode ($\upsilon_3$) and the two non-degenerate bending modes (δ_1 and δ_2). Their IR spectra results of the physiadsorbed CO_2 samples show the shift from the free CO_2 peak (2349 cm^{-1}) in the asymmetric stretching mode. They identified that several reasons may contribute to the frequency shift, which the three most important factors, including the elongated CO_2 molecule i.e. change in the molecule length, the off-center asymmetric distortion of the carbon atoms of CO_2, and the effect of the metal center. By analyzing the geometries of the absorbed CO_2, they noticed that the absorbed CO_2 molecules have been distorted from their free molecule geometry, affecting an off-center shift of the carbon atom, as well as an elongated overall length of the molecule. In case of the effect of the metal center, the nearby open metal center might also play a direct role in the frequency shift, by attracting or repelling the nearby oxygen atom in the CO_2 molecules during the vibration. Hence, these factors can cause in different effects on the frequency (blueshift or redshift) of the asymmetric stretch.

Recently, Gabrienko et al. (2016) found the band of sorbed CO_2 after subjected to high-pressure CO_2 at ~2334 cm^{-1} and ~2323 cm^{-1} which are assigned to the v_3 asymmetric stretching, and hot band $(v_3 + v_2) – v_2$, respectively.

From our results, the resolved IR bands of the asymmetric CO_2 stretch mode, 2400-2300 cm^{-1}, can also serve as an indication of the sorption of CO_2 to the BC-based samples (Figure 32-34). This spectral region contains the contributions of the fundamental C=O asymmetric stretching vibrational modes v_3 for the CO_2. Table 4 summarizes the vibrational band positions in the asymmetric stretching region of sorbed CO_2 from the deconvoluted BC-based membrane spectra. The FTIR absorption spectra of the samples in Figure 35-37 are quite complex showing the presence of several spitting bands in both control and CO_2 pressurized conditions. Nevertheless, the IR absorption intensity can be notably enhanced after exposure to CO_2 which implies the taking part of CO_2 with the membrane samples. Generally, asymmetric stretching vibration of CO_2 is around 2350 cm^{-1} (“Engineering Chemistry 1 – Photochemistry and spectroscopy, Unit 3 Spectroscopy Lecture Notes”, 2013). On the other hand, Oancea et al. (2012) reported that the gaseous CO_2 at room temperature and 1 bar pressure usually show a double absorption band at ~2360 and ~2340 cm^{-1} that are, in fact, the envelopes for the number of rotational transitions that occur for the asymmetric stretching band.

Figure 35 illustrates the resolved IR absorption spectra of the basic BC samples for the control and 16h exposure to CO_2 conditions. As can be seen, the shape of the spectral line changes obviously after pressurization. The CO_2 sorption of the pressurized BC sample was determined by the remarkable IR absorption bands presented in Figure 35, where the spectrum of the control BC sample reveals weak bands and are almost the same intensity. As a result, there is no outstanding peak obtained from the control spectrum (Figure 35). On the contrary, much more higher intensity of v_3 CO_2 absorbance obtained from the spectrum of the BC sample after pressurization 16h. Several additional lines were found in both spectrum in this region. However, the band at ~2360 cm^{-1} is the most distinguished peak for the pressurized BC sample suggesting owing to the gaseous CO_2 (Figure 35). Further, other splitting bands from both control and pressurized BC spectrum due to the CO_2 sorption are presented in Table 4. The hot band $(v_3 + v_2) – v_2$ at ~2323 cm^{-1} was also found in agreement with Gabrienko et al. (2016), which arises when the rotational motion is impeded due to interaction with the environment (Cunliffe-Jones, 1969), becomes more pronounced after CO_2 exposure (Figure 35). Usually, this band is positioned at lower frequencies (by about 12 cm^{-1}) with respect to v_3 band (Cunliffe-Jones, 1969). Compared to the control BC spectrum, it was found that some appeared splitting peaks shifted after being exposure to CO_2 16h (Figure 35). This can be suggested the ability of the sample to interact with CO_2 molecules. It should also be mentioned that the shift of the asymmetric stretch (v_3) band was also observed when the CO_2 was trapped into solid I-clathrate hydrates (Oancea et al. 2012).

Table 4. Carbon dioxide asymmetric stretching vibrational band positions from the from the deconvoluted BC-based membrane spectra.

Membranes	**Splitting bands in the CO_2 asymmetric stretching region (cm^{-1})**
BC+Teflon	
- Control	2369.1, 2362.4, 2354.7, 2345, 2341.2, 2334.4, 2324.8, 2317.1
- 16h CO_2 pressurized	2370.1, 2360.4, 2354.7, 2344.1, 2339.2, 2334.4, 2325.7, 2317.1
BC+Silk+Teflon	
- Control	2369.1, 2357.6, 2348.9, 2341.2, 2334.4, 2323.8, 2316.1
- 24h CO_2 pressurized	2367.2, 2356.6, 2343.1, 2331.5, 2323.8, 2310.3
BC+ZnO+Teflon	
- Control	2370.1, 2362.4, 2354.7, 2349.8, 2347.9, 2343.1, 2334.4, 2323.8, 2313.2
- 24h CO_2 pressurized	2373.9, 2365.3, 2360.4, 2354.7, 2344.1, 2337.3, 2336.3, 2323.8, 2317.1

Moreover, several stand out additional lines and broader bands were noticed, particularly in the case of silk fibroin- and ZnO- modified BC membranes as illustrated in Figure 36 and 37. As can be seen (Figure 36 and 37), the spectrum of silk fibroin-modified BC sample after pressurization 24h provides the three distinguished bands at 2356 cm^{-1}, 2343 cm^{-1}, 2323 cm^{-1} (Figure 36), as well as the broad and various prominent bands of ZnO-modified BC sample after CO_2 exposure 24h (Figure 37) are the good evidence for the presence of sorbed CO_2 with different sites of the membranes. The other splitting peaks of these spectra are detailed in Table 4. In accordance with the demonstration of broader and extra splitting bands of the silk fibroin- and ZnO-modified BC membranes spectra (Figure 36 and 37), which is similar to the bending absorption bands region, this evidence can be signified the introduction of silk fibroin and ZnO nanoparticles into BC matrix increase the number of active sites for interaction with CO_2. The appearance of the additional peaks is the consequence of the presence of more inequivalent sites for the CO_2 adsorption. In addition, the more intense absorption bands are obtained from the samples after exposure to CO_2. These results are consistent with Shieh and Liu (2003) and Yamakawa et al. (2016) who reported the IR absorption spectra of CO_2 sorption by their samples. Shieh and Liu (2003) revealed IR absorption spectrum of CO_2 impregnated into PC film, they noticed very broad of absorption bands at 2338 cm^{-1} and 2326 cm^{-1}. They thus indicated that more than one type of the site within the PC matrix is available for CO_2 molecules which includes carbonyl groups and benzene rings. In the case of the CO_2 interaction with PMMA polymer (where the carbonyl was the only active functional group), a single v_3 asymmetric stretching peak was obtained (Kazarian et al., 1996). Yamakawa et al. (2016) carried out IR spectra of CO_2 on titania nanotubes and observed absorption peaks at 2350 cm^{-1} and 2340 cm^{-1} assigned them to v_3 of CO_2 physisorbed at two different kinds of sites on the titania nanotubes because their frequencies are close to the gas phase value of 2349.3 cm^{-1}. They also found another absorption peak at 2372 cm^{-1} that was attributed to the combination band of v_3 and the external vibrational mode of CO_2 against the surfaces of titania nanotubes.

According to the assignment of some peak positions in this region from other studies as mention above, we suggested that the peak positioned at ~2370 cm^{-1}, ~2360 cm^{-1} and ~2340 cm^{-1}, ~2350 cm^{-1}, ~2334 cm^{-1}, and ~2323 cm^{-1} are corresponding to the combination band of υ_3 and the external vibrational mode of CO_2 against the surfaces of membrane, gas phase of CO_2, physically sorbed CO_2, asymmetric stretching vibration of CO_2, and hot band. In conclusion, based on our FTIR spectra in the v_3 region of CO_2, the presence of several absorption bands of all BC-based membranes are responsible for a mixture of bound CO_2 with different basic sites and gaseous CO_2 (Freund and Roberts, 1996).

Besides, the OH vibrational region was considered whether it changes after incorporation with CO_2. It is note that the consideration of this region was only for the basic BC membranes since the other modified BC membranes could not exclude the effect of matrix-filler interactions. A slightly shift of OH stretching vibration IR peak towards higher wavenumber of the samples after reaction with CO_2 was noticed (data not shown). The control BC sample presented at 3336 cm^{-1}, while the other entrapped CO_2 BC samples show the peak at 3338 cm^{-1}, 3341 cm^{-1}, and 3337 cm^{-1} for 8h, 16h, and 24h, respectively. This shifts are responsible for the Lewis acid–base kind of interaction between OH group and CO_2 as already reported by Nalawade et al. (2006) that their functional groups in polymers interacted with CO_2 and demonstrated the shifts of the functional group vibrational band to higher wavenumber.

Hydroxyl group (-OH) within the BC-based membrane matrix is a functional group wherein the oxygen atom serves as an electron-donor center, thus it can interact with CO_2 (Yang et al., 2016). Also, Liu and Wilcox (2012) claimed that the oxygen-containing functional groups, especially in the case of hydroxyl and carbonyl groups increase the adsorbed CO_2 by the electronic structure prediction owing to the higher electron densities surrounding the oxygen atoms of those functional groups attract CO_2. Therefore, we demonstrate the possible reaction mechanisms of the interaction of the CO_2 with, cellulose, silk fibroin and ZnO nanoparticles in Figure 38.

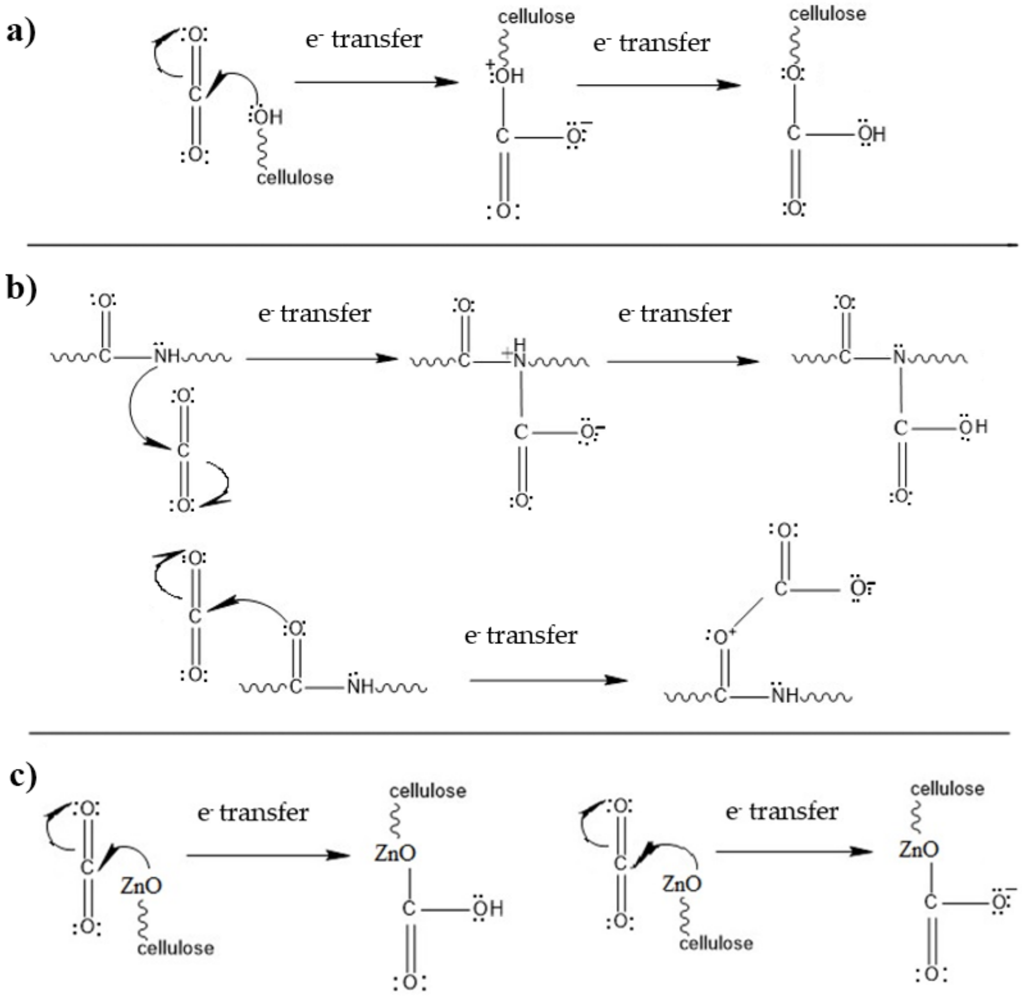

Figure 38. Possible mechanisms of the interactions of the CO_2 with a) BC (hydroxyl), b) silk fibroin (amide) functional groups, and c) ZnO nanoparticles (formation of the bicarbonate (left) and monodentate carbonate species (right)) (Galhotra and Grassian, 2010).

Our results suggest that the interaction of the CO_2 and the membrane is mostly Lewis acid-base type of interaction. However, we cannot exclude the possibility that there is a contribution from the dipole-quadrupole interactions between polar groups within the membranes and CO_2 (Huang, 1973; Nalawade et al., 2006). Even though the dipole moment for CO_2 is zero, the quadrupole moment is not (Kim and Kim, 2008). Due to its highly electronegative oxygen atoms, CO_2 has a considerable quadrupole moment, which is a distribution of electric charge of four equal monopoles or two equal dipoles arranged close together with alternating polarity (“Quadrupole”, 2016). The spectra of the CO_2 bending and asymmetric stretching vibration modes presented clearly suggest that there is an interaction of CO_2 with the membrane material. The proposed mechanisms of the interaction of the CO_2 with cellulose, silk fibroin, and ZnO nanoparticles are presented in Figure 38. As can be seen in Figure 38(a), CO_2 could react with a large number of hydroxyl groups from BC that act as Lewis bases or electron donors. First, the carbon atom from CO_2 accepts the electron-pair from the hydroxyl group and the oxygen from the OH group becomes partially positive. After that, the electrons are transferred to one of the oxygen atoms in CO_2, which becomes partially negative. The negatively charged oxygen atom then could form intra or inter hydrogen bonding with cellulose. Figure 38(b) shows the possible mechanism between the amide bond and a CO_2 molecule. It is similar to the BC-CO_2 interaction, but the amide bond provides two sites (C=O and NH groups) for the interaction with CO_2. It means that the blending of the BC with silk fibroin could enhance the chance to interact with CO_2. The experiments on the adsorption of the CO_2 on ZnO surface and the quantum chemical calculations suggested that there were several mechanisms of CO_2-ZnO interaction, which results in formation of bent CO_2, bicarbonate, carbonate (monodentate and bidentate) and carboxylate species (Galhotra and Grassian, 2010). Bicarbonate formation occurs with an initial nucleophilic attack of CO_2 on the metal oxide surface followed by an intermolecular proton transfer (Figure 38(c) left) (Galhotra and Grassian, 2010). A suggested mechanism for the formation of monodentate species is depicted on the right hand side of Figure 38(c).

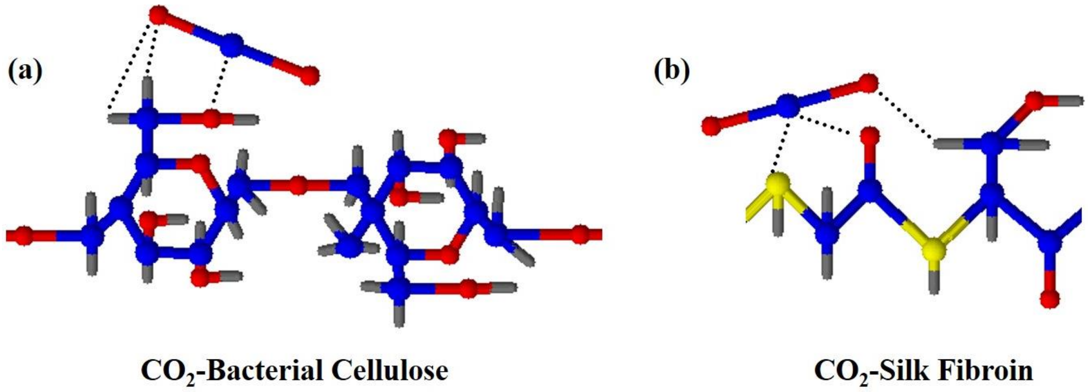

Figure 39. Possible complexes of CO_2 with (a) bacterial cellulose and with (b) silk fibroin; blue, red, yellow, and gray spheres represented as carbon, oxygen, nitrogen, and hydrogen atoms, respectively.

Figure 39 demonstrates one of the possible complex structures of CO_2-bacterial cellulose and CO_2-silk fibroin. The different configurations depend on the location of CO_2 bound to bacterial cellulose and silk fibroin. From the proposed structures (Figure 39), CO_2 is able to bind to the hydroxyl group and amide bond by Lewis acid-Lewis base interaction and bind to electron-deficient C-H bonds from bacterial cellulose/silk fibroin by a cooperative weak hydrogen bond. The partial negatively charges oxygen atoms of CO_2 can be involved in weak electrostatic interactions with C-H bonds, thus form a cooperative weak hydrogen bond C-H●●●O (Kim and Kim, 2008).

3.3.3 Carbonate Species Vibrational Region

The adsorption of CO_2 by the BC-based membrane materials may also results in the formation of complex species in IR absorption region of 1700-1200 cm^{-1}. In accordance with the suggested reaction mechanisms (Figure 38), the different carbonate species are able to form after being exposed to CO_2. The IR absorption bands of those species are considered in 1700-1200 cm^{-1} region as illustrated in Figure 40 (Galhotra and Grassian, 2010). The species could be found after interaction with CO_2 include linearly adsorbed CO_2, carbonate, bicarbonate, and carboxylate species (Baltrusaitis et al., 2011). However, linearly adsorbed CO_2 exhibits asymmetric stretch (υ_3) in the spectral region of 2400 –2300 cm^{-1} that we already discussed in the section of asymmetric stretching (υ_3) vibration mode of CO_2. Galhotra and Grassian (2010) investigated the adsorption of CO_2 on the ZnO surface by the FTIR spectroscopy and found the peaks at 1225 cm^{-1}, 1442 cm^{-1}, and 1630 cm^{-1} which are distinctive of the bicarbonate species formation. In addition to the bicarbonate peaks, they also noticed a number of other peaks are in the spectra that appear at 1475 and 1377 cm^{-1} are due to O-C-O stretching vibrations of the monodentate carbonates species, and the adsorption bands at 1606 cm^{-1} and 1334 cm^{-1} are assigned to OCO stretching, both symmetric and asymmetric stretching, of bidentate carbonate species.

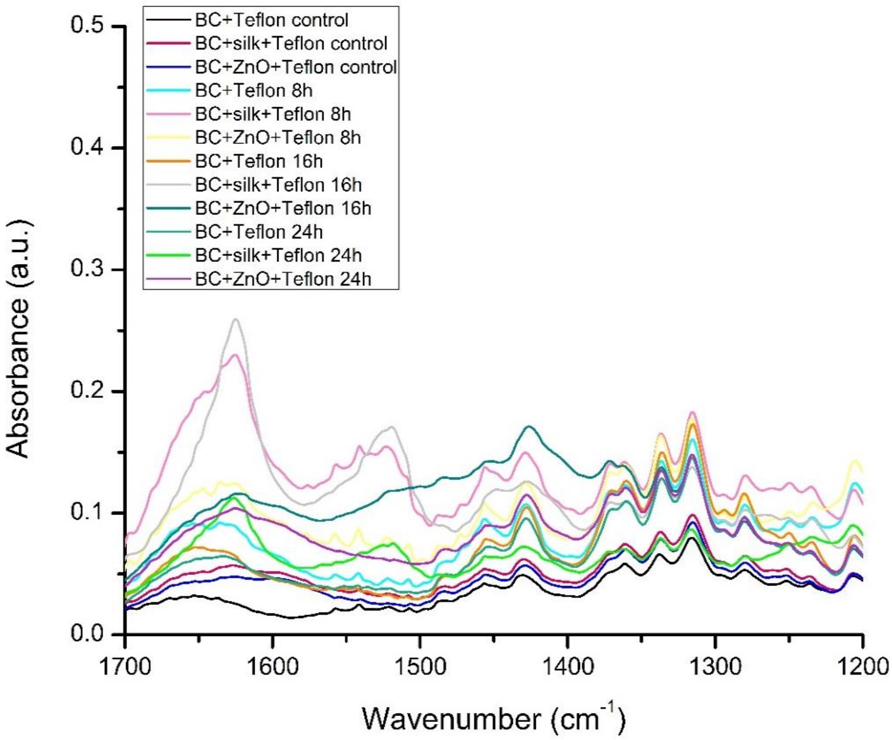

Figure 40. ATR-FTIR spectra of BC-based membranes in the range of 1700-1200 cm^{-1}.

Considering the absorbance peaks in this region (Figure 40) that are responsible for the range of carbonate species vibrations (Galhotra and Grassian, 2010), the absorbance intensity increases after incorporation with CO_2. This implies that there are probably some carbonate species formed after pressurization with CO_2 as the supposed mechanisms in Figure 38. According to those mechanisms, bicarbonate species and monodentate carbonate species should be formed after interaction with CO_2. Nevertheless, the absorption bands in 1700-1200 cm^{-1} region are ambiguous to identify the types of the adsorbed carbonate species formation since their vibrational region is located in the same region as the IR absorption bands of cellulose and silk fibroin characteristics. All of the surface bound carbonate species vibrational bands fall in the same position as vibrational bands of some bonds from bacterial cellulose and silk fibroin.

3.3.4 Integrated Area under IR Absorption Bands of CO_2 Vibrational Modes

To further justify the conclusion, determination of integrated area of IR absorption spectral bands of CO_2 are useful for the quantification results. It should be note that this method is simple to obtain the relative CO_2 attachment content with our membrane samples, owing to ATR-FTIR spectroscopy measurement can provides quantitative information from the recorded spectra (Gabrienko et al., 2016). This agrees with Krukowski et al. (2015) and Tan and Ni (1997). According to the Beer-Lambert law, the spectral band absorbance is proportional to the concentrations of the attenuating species in the material sample (“Beer–Lambert law”, 2017). The concentrations of the surface adsorbed species in the material sample (surface concentration) is related to the IR absorbance peak areas by the integrated Beer-Lambert relation (Tan and Ni, 1997). We have then integrated the areas of two vibrational regions of CO_2; 689-644 cm^{-1} and 2375-2310 cm^{-1}, for all samples which were assigned to the bending and asymmetric stretching mode, respectively. Figure 41 summarizes the plots between integrated area of IR bands from the CO_2 bending (v_2) mode and CO_2 asymmetric stretching (v_3) mode versus the conditions of the membranes; control and after introduction of CO_2 to BC-based samples in various time (8h, 16h, 24h). The control sample means no exposure to CO_2 3 bars, whereas, being removed CO_2 by heating above 100°C.

It was clearly noticed from Figure 41(a) and 41(b) regarding the enhancement of the integrated absorption band areas from both vibrational modes indicating an increase of the amount of sorbed CO_2 on the membranes after pressurization with CO_2. Overall, basic BC membrane, silk fibroin-modified BC membrane and ZnO nanoparticles-modified BC membrane were able to achieve the highest efficiency at 16h and 8h after CO_2 sorption, respectively. In response to a comparison of the CO_2 spectral areas in Figure 41(a) and 41 (b), it can be mentioned that the highest relative CO_2 sorption quantity was obtained from ZnO nanoparticles-modified BC membrane after CO_2 affiliation 8h.

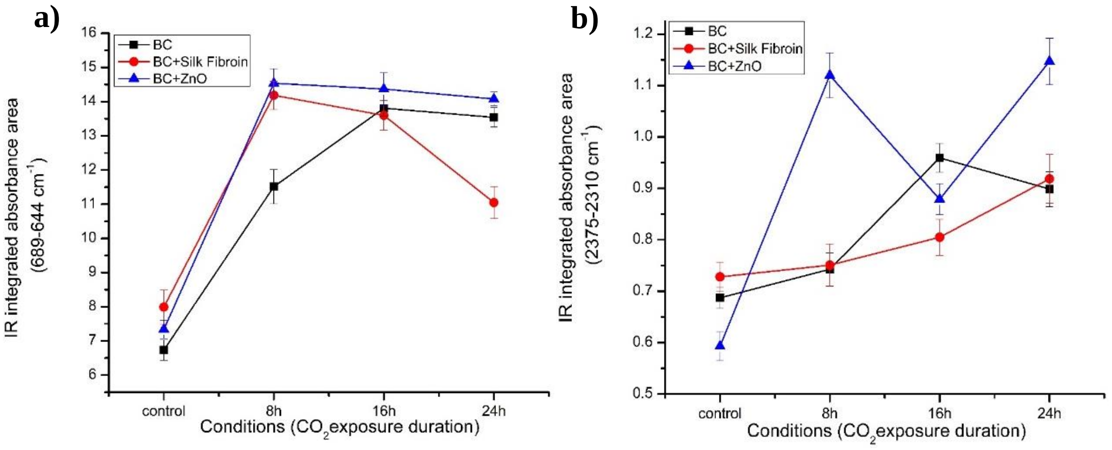

Figure 41. Integrated area of; a) the v_2 CO_2 bending (689-644 cm^{-1}) absorption bands and b) the v_3 CO_2 asymmetric stretching (2375-2310 cm^{-1}) absorption bands versus conditions of CO_2 exposure (control, 8h, 16h, and 24h).

As can be observed in Figure 41(a), the CO_2 bending feature areas greatly increase from the control to 8h condition in case of the modified BC membranes, defining abundant of sorbed CO_2 presented. Regarding to the basic BC membrane, its CO_2 spectral areas enhance gradually from the control. This signified that the ability to interact with CO_2 by the modified membranes was more rapid than that of the basic BC membrane. Consequently, it can be mentioned that CO_2 adsorption is facilitated by modification with silk fibroin and ZnO nanoparticles. This was expected owing to the presence of various active sites from silk fibroin and ZnO nanoparticles.

A decrease of CO_2 asymmetric stretching band areas of the ZnO-modified BC membrane at 16h duration in Figure 41(b) were supposed that the affiliated CO_2 with this membrane preferred to vibrate in the bending motion instead of the asymmetric stretching. Additionally, it can be found that the bound CO_2 with silk fibroin-modified BC membrane after 8h condition was able to vibrate in asymmetric stretching mode increasingly.

In conclusions, the modified BC membranes offers the greatest capability to capture CO_2 and ZnO nanoparticles-modified BC membrane seems suitable for a longer time adsorption with respect to the other membranes. The basic BC membrane and ZnO nanoparticles modified BC membrane were probably saturated by CO_2 since 16h and 8h exposure time respectively.

CHAPTER IV

CONCLUSIONS

Main Conclusions of This Research Work

The main conclusions of this work can be summarized as follows:

1. Bacterial cellulose (BC)-based membranes were successfully fabricated via normal casting evaporation drying technique using bacterial cellulose from *Nata de coco* as membrane matrix. The addition of silk fibroin and ZnO nanoparticles into the BC matrix, so-called silk fibroin- and ZnO nanoparticles-modified BC membrane, was able to increase the number of specific sites for interaction with CO_2 as proved by the results from ATR-FTIR study.

2. The results from structural analysis by FTIR spectroscopy demonstrated that there was no important bands changed and no new covalent bonds for the modified BC membranes. While, the modified BC membranes spectra show only some peaks shifted and extra peaks from either silk fibroin or ZnO nanoparticles characteristics compared to the basic BC membrane.

3. The FESEM analysis shows mesh network nanofibrils structure with the distribution of pores in nano-size of all BC-based membranes.

4. From the ATR- FTIR spectroscopy studies of the interaction of the BC-based membranes with CO_2, it has been found that an increase in the absorbance of CO_2 bending and asymmetric stretching IR envelopes after pressurization, the appearance of additional bands, and the presence of several splitting bands could be confirmed the CO_2 sorption to the membranes. The Lewis acid-base type of interaction was supposed to be a main interaction. However, we do not have conclusive spectroscopic evidence for which types of adsorbed carbonate species formed since their vibrations are located in the same region as cellulose and silk fibroin charateristics.

5. It is noteworthy that the modified BC membranes provide the optimum ability to capture CO_2 by displaying broader and more splitting peaks in both vibrational modes of CO_2. The general conclusion is that CO_2 interact strongly with BC-based membrane materials and that adsorption can be facilitated by the active sites from silk fibroin and ZnO nanoparticles.

Acknowledgements

First of all, I would like to acknowledge the financial support of the Balassi Institute and the Hungarian Scholarship Board (HSB) through my PhD studies. This research was carried out in the Institute of Wood Based Products and Technologies, Simonyi Karoly Faculty of Engineering, Wood Sciences and Applied Arts at University of West Hungary during 2014-2017. The work was accomplished as partial fulfillment of the requirements for the degree of doctor of philosophy. I am thankful to Thongaumphai's production (Thailand) for providing raw *Nata de coco* during the experiment.

My deep gratitude also goes to my research supervisor, Prof. Dr. Levente Csóka, who gave me the opportunity to study and do this research. He expertly guided me as well as took care of me through the entire studies. I am really appreciated to his kindness. His valuable advice and suggestions brought this research to be succeeded. Without his guidance and help, this dissertation would not have been possible. It is a great honor to work under his supervision.

I would also like to thank Dr. Katalin Halász, Adam Makk, and Eva Papp for their helps and suggestions during my studies. I sincerely thank the official and other staffs for helping me to accomplish this work.

Last but not least, I also wish to thank my beloved parents; Narin-Wanna Hosakun, lovely sister; Worakan Hosakun, and friends for their inspiration, understanding, encouragement, love, advices, and support.

List of My Publications

- Yanin Hosakun, Katalin Halász, Miklos Horváth, Levente Csóka, and Vladimir Djoković. “ATR-FTIR Study of the Interaction of CO_2 with Bacterial cellulose-Based Membranes” (submitted).

- Katalin Halász, Yanin Hosakun, and Levente Csóka. “Reducing Water Vapor Permeability of Poly(lactic acid) Film and Bottle through Layer-by-Layer Deposition of Green-Processed Cellulose Nanocrystals and Chitosan,” International Journal of Polymer Science, vol. 2015, 6 pages, 2015.

- Yanin Hosakun, Katalin Halász, Miklos Horváth, Levente Csóka, and Vladimir Djoković “ATR-FTIR Study of the Interaction of CO_2 with Bacterial cellulose-Based Membranes” COST Action FP1205: Innovative Applications of Regenerated Wood Cellulose Fibres, Stockholm, Sweden.

- Yanin Hosakun, Sujitra Wongkasemjit, and Thanyalak Chaisuwan “Preparation of Bacterial Cellulose Membranes from Nata de coco for CO_2/CH_4 Separation” ICCEE 2014: International Conference on Chemical and Environmental Engineering, Barcelona, Spain.

- Yanin Hosakun, Sujitra Wongkasemjit, and Thanyalak Chaisuwan “Preparation of Bacterial Cellulose Membranes from Nata de coco with and without Silver Ions for CO_2/CH_4 Separation” The 5th Research Symposium on Petrochemical and Materials Technology and The 20th PPC Symposium on Petroleum, Petrochemicals and Polymers, Bangkok, Thailand.

CHAPTER V

REFERENCES

1. A blanket around the Earth. (2016, December). Retrieved from http://climate.nasa.gov/causes/

2. Abedini, R.; Nezhadmoghadam, A. Application of membrane in gas separation processes: Its suitability and mechanisms. Petroleum and Coal 2010.

3. Albu, M.G.; Vuluga, Z.; Panaitescu, D.M.; Vuluga, D.M.; Căşărică, A.; Ghiurea, M. Morphology and thermal stability of bacterial cellulose/collagen composites. Central European Journal of Chemistry 2014, 12, 968-975.

4. Anderson, S.; Newell, R. Prospects for carbon capture and storage technologies. Annual Review of Environment and Resources 2004, 29, 109-142.

5. Baker, R.W.; Lokhandwala, K. Natural gas processing with membranes: An overview. Industrial & Engineering Chemistry Research 2008, 47, 2109-2121.

6. Baltrusaitis, J.; Schuttlefield, J.; Zeitler, E.; Grassian, V.H. Carbon dioxide adsorption on oxide nanoparticle surfaces. Chemical Engineering Journal 2011, 170, 471-481.

7. Beer–Lambert law. (2017, January, 6). Retrieved from https://en.wikipedia.org/wiki/Beer%E2%80%93Lambert_law

8. Berger, A.H.; Bhown, A.S. Comparing physisorption and chemisorption solid sorbents for use separating CO_2 from flue gas using temperature swing adsorption. Energy Procedia 2011, 4, 562-567.

9. Bernardo, P.; Clarizia, G. 30 Years of Membrane Technology for Gas Separation. Chemical Engineering Transactions 2013, 32, 1999-2004.

10. Bunnell, J. Silk Fibroin. Retrieved from https://www.tes.com/lessons/xgx8VfOSYlkF4w/silk-fibroin

11. Carbon Dioxide. (2016, October). Retrieved from http://climate.nasa.gov/vital-signs/carbon-dioxide/

12. Chung, T.-S.; Jiang, L.Y.; Li, Y.; Kulprathipanja, S. Mixed matrix membranes (mmms) comprising organic polymers with dispersed inorganic fillers for gas separation. Progress in Polymer Science 2007, 32, 483-507.

13. CO_2 Capture Methods. Retrieved from http://www.esru.strath.ac.uk/EandE/Web_sites/02-03/carbon_sequestration/Carbon%20Sequestration-422.htm

14. Cong, H.; Radosz, M.; Towler, B.F.; Shen, Y. Polymer–inorganic nanocomposite membranes for gas separation. Separation and Purification Technology 2007, 55, 281-291.

15. Cunliffe-Jones, D.B. Perturbation of Some Vibrational Bands in Solution. Spectrochimica Acta Part A: Molecular Spectroscopy 1969, 25, 779-791.

16. Danten, Y.; Tassaing, T.; Besnard, M. Ab initio investigation of vibrational spectra of water−($CO_2)_n$ complexes (n = 1, 2). The Journal of Physical Chemistry A 2005, 109, 3250-3256.

17. Djaja, N.F.; Montja, D.A.; Saleh, R. The Effect of CO Incorporation into ZnO Nanoparticles. Advances in Materials Physics and Chemistry 2013. 3(1), 33-41.

18. Djurisic, A.B.; Chen, X.; Leung, Y.H.; Man Ching Ng, A. Zno nanostructures: Growth, properties and applications. Journal of Materials Chemistry 2012, 22, 6526-6535.

19. El-Azzami, L.A.; Grulke, E.A. Carbon dioxide separation from hydrogen and nitrogen by fixed facilitated transport in swollen chitosan membranes. Journal of Membrane Science 2008, 323, 225-234.

20. Engineering Chemistry 1 - PHOTOCHEMISTRY AND SPECTROSCOPY (Unit 3 Spectroscopy) Lecture Notes; Anna University. (2013, DEC, 14). Retrieved from http://tnupdater.blogspot.hu/2013/12/cy6151-engineering-chemistry-1.html.

21. Esa, F.; Tasirin, S.M.; Rahman, N.A. Overview of bacterial cellulose production and application. Agriculture and Agricultural Science Procedia 2014, 2, 113-119.

22. Fan, M.; Dai, D.; Huang, B. Fourier Transform Infrared Spectroscopy for Natural Fibres. Fourier Transform - Materials Analysis. Dr Salih Salih (Ed.), InTech 2012. Retrieved from http://www.intechopen.com/books/fourier-transform-materials-analysis/fourier-transform-infrared-spectroscopy-for-natural-fibres

23. Farias, S.A.S.; Longo, E.; Gargano, R.; Martins, J.B.L. CO_2 adsorption on polar surfaces of ZnO. Journal of Molecular Modeling 2013, 19, 2069-2078.

24. Fibroin. (2015, February, 10). Retrieved from http://en.wikipedia.org/wiki/Fibroin#mediaviewer/File:Silk_fibroin_primary_structure.svg

25. Francisco, G.J.; Chakma, A.; Feng, X. Separation of carbon dioxide from nitrogen using diethanolamine-impregnated poly(vinyl alcohol) membranes. Separation and Purification Technology 2010, 71, 205-213.

26. Freund, H.J.; Roberts, M.W. Surface chemistry of carbon dioxide. Surface Science Reports 1996, 25, 225-273.

27. Gabrienko, A.A.; Ewing, A.V.; Chibiryaev, A.M.; Agafontsev, A.M.; Dubkov, K.A.; Kazarian, S.G. New insights into the mechanism of interaction between CO_2 and polymers from thermodynamic parameters obtained by in situ ATR-FTIR spectroscopy. Physical Chemistry Chemical Physics 2016, 18, 6465-6475.

28. Galhotra, P.; Grassian, V.H. Carbon dioxide adsorption on nanomaterials. Ph. D. thesis. Department of Chemistry 2010, University of Iowa.

29. Gantzel, P.K.; Merten, U. Gas separations with high-flux cellulose acetate membranes. Industrial & Engineering Chemistry Process Design and Development 1970, 9, 331-332.

30. Global Temperature. (2015). Retrieved from http://climate.nasa.gov/vital-signs/global-temperature/

31. Hafeez, S.; Fan, X.; Hussain, A. A Kinetic Study of CO_2 Adsorption in Cellulose Acetate Membranes. International Journal of Environmental Science and Development 2015, 6(10), 755-759.

32. Hafeez, S.; Fan, X.; Hussain, A.; Martín, C.F. CO_2 adsorption using TiO_2 composite polymeric membranes: A kinetic study. Journal of Environmental Sciences 2015, 35, 163-171.

33. He, X.; Hägg, M.-B. Membranes for Environmentally Friendly Energy Processes. Membranes 2012, 2, 706-726.

34. Huang, Y.-Y. Quadrupole interaction of carbon dioxide on silica-alumina surface. The Journal of Physical Chemistry 1973, 77 (1), 103-106.

35. Hu, W.; Chen, S.; Li, X.; Shi, S.; Shen, W.; Zhang, X.; Wang, H. In situ synthesis of silver chloride nanoparticles into bacterial cellulose membranes. Materials Science and Engineering: C 2009, 29, 1216-1219.

36. Hu, W.; Chen, S.; Zhou, B.; Wang, H. Facile synthesis of ZnO nanoparticles based on bacterial cellulose. Materials Science and Engineering: B 2010, 170, 88-92.

37. Infrared Spectroscopy. Retrieved from http://www.chem.ucla.edu/~harding/notes/notes_14C_IR.pdf

38. Introduction to Lewis acid-base chemistry. Retrieved from https://www.utdallas.edu/~scortes/ochem/OChem1_Lecture/Class_Materials/12_lewis_ac_bases.pdf

39. Jamróz, M.H.; Dobrowolski, J.C.; Bajdor, K.; Borowiak, M.A. Ab initio study of the $\nu(CO_2)$ mode in EDA complexes. Journal of Molecular Structure 1995, 349, 9-12.

40. Jonas, R.; Farah, L.F. Production and application of microbial cellulose. Polymer Degradation and Stability 1998, 59, 101-106.

41. Jung, R.; Jin, H. J. Preparation of Silk Fibroin/Bacterial Cellulose Composite Films and Their Mechanical Properties. Key Engineering Materials, 2007, 342-343, 741-744.

42. Kasturirangan, A. Specific Interactions in Carbon Dioxide + Polymer Systems. Ph.D. Thesis, Georgia Institute of Technology, Georgia. December 2007.

43. Kazarian, S.G.; Vincent, M.F.; Bright, F.V.; Liotta, C.L.; Eckert, C.A. Specific Intermolecular Interaction of Carbon Dioxide with Polymers. Journal of the American Chemical Society 1996, 118, 1729-1736.

44. Keshk, S.MAS. Bacterial Cellulose Production and its Industrial Applications. Journal of Bioprocessing & Biotechniques 4. 2014, 4(2), 150.

45. Khan, A. Development of cellulose nanocrystal reinforced antimicrobial nanocomposite films for food packaging application. Ph.D. Thesis. University of Quebec, National Institute of Scientific Research. October 2014.

46. Kim, K.H.; Kim, Y. Theoretical studies for Lewis acid−base interactions and C−H···O weak hydrogen bonding in various CO_2 complexes. The Journal of Physical Chemistry A 2008, 112, 1596-1603.

47. Koh, L.-D.; Cheng, Y.; Teng, C.-P.; Khin, Y.-W.; Loh, X.-J.; Tee, S.-Y.; Low, M.; Ye, E.; Yu, H.-D.; Zhang, Y.-W., et al. Structures, mechanical properties and applications of silk fibroin materials. Progress in Polymer Science 2015, 46, 86-110.

48. Koteeswaran, M. CO_2 and H_2S corrosion in oil pipelines. Master's Thesis. Faculty of Mathematics and Natural Science, University of Stavanger. June 2010.

49. Kothandaraman, A. Carbon Dioxide Capture by Chemical Absorption: A Solvent Comparison Study. Ph.D. Thesis. Department of Chemical Engineering, Massachusetts Institute of Technology. June 2010.

50. Krukowski, E.G.; Goodman, A.; Rother, G.; Ilton, E.S.; Guthrie, G.; Bodnar, R.J. Ft-ir study of CO_2 interaction with na+ exchanged montmorillonite. Applied Clay Science 2015, 114, 61-68.

51. Lavalley, J.C.; Saussey, J.; Bovet, C. Infrared spectroscopic study of the CO_2 adsorption effect on the surface acidity of zinc oxide. Journal of Molecular Structure 1982, 80, 191-194.

52. Legnani, C.; Vilani, C.; Calil, V.L.; Barud, H.S.; Quirino, W.G.; Achete, C.A.; Ribeiro, S.J.L.; Cremona, M. Bacterial cellulose membrane as flexible substrate for organic light emitting devices. Thin Solid Films 2008, 517, 1016-1020.

53. Li, B.; Duan, Y.; Luebke, D.; Morreale, B. Advances in CO_2 capture technology: A patent review. Applied Energy 2013, 102, 1439-1447.

54. Lin, H.; Freeman, B.D. Gas permeation and diffusion in cross-linked poly(ethylene glycol diacrylate). Macromolecules 2006, 39, 3568-3580.

55. Lin, K.-Y.A.; Park, A.-H.A. Effects of Bonding Types and Functional Groups on CO_2 Capture using Novel Multiphase Systems of Liquid-like Nanoparticle Organic Hybrid Materials. Environmental Science & Technology 2011, 45, 6633-6639.

56. Liu, X.; Zhang, K.-Q. Silk fiber — molecular formation mechanism, structure-property relationship and advanced applications. 2014.

57. Liu, Y.; Wilcox, J. Effects of surface heterogeneity on the adsorption of CO_2 in microporous carbons. Environmental Science & Technology 2012, 46, 1940-1947.

58. Martinez, C. R.; Joshi, P.; Vera, J.L.; Ramirez -Vick, J.E.; Perales, O.; Singh, S.P. Cytotoxic studies of PEG functionalized ZnO nanoparticles on MCF-7 cancer cells. NSTI Nanotechnology Conference and Expo, NSTI-Nanotech 2011, 3, 420-423.

59. Ming, J.; Liu, Z.; Bie, S.; Zhang, F.; Zuo, B. Novel silk fibroin films prepared by formic acid/hydroxyapatite dissolution method. Materials Science and Engineering: C 2014, 37, 48-53.

60. Mitropoulos, A. N.; Marelli, B.; Ghezzi, C. E.; Applegate, M. B.; Partlow, B. P.; Kaplan, D. L.; Omenetto, F. G. Transparent, Nanostructured Silk Fibroin

Hydrogels with Tunable Mechanical Properties. ACS Biomaterials Science & Engineering 2015, 1 (10), 964-970.

61. Moore, T.T.; Koros, W.J. Non-ideal effects in organic–inorganic materials for gas separation membranes. Journal of Molecular Structure 2005, 739, 87-98.

62. Nalawade, S.P.; Picchioni, F.; Marsman, J.H.; Janssen, L.P.B.M. The FT-IR studies of the interactions of CO_2 and polymers having different chain groups. The Journal of Supercritical Fluids 2006, 36, 236-244.

63. Oancea, A.; Grasset, O.; Le Menn, E.; Bollengier, O.; Bezacier, L.; Le Mouélic, S.; Tobie, G. Laboratory infrared reflection spectrum of carbon dioxide clathrate hydrates for astrophysical remote sensing applications. Icarus 2012, 221, 900–910.

64. Oliveira Barud, H. G.; Barud, H. d. S.; Cavicchioli, M.; do Amaral, T. S.; Junior, O. B. d. O.; Santos, D. M.; Petersen, A. L. d. O. A.; Celes, F.; Borges, V. M.; de Oliveira, C. I.; de Oliveira, P. F.; Furtado, R. A.; Tavares, D. C.; Ribeiro, S. J. L. Preparation and characterization of a bacterial cellulose/silk fibroin sponge scaffold for tissue regeneration. Carbohydrate Polymers 2015, 128, 41-51.

65. Overview of Greenhouse Gases. (2016, october 6). Retrieved from https://www.epa.gov/ghgemissions/overview-greenhouse-gases

66. Palme, A.; Theliander, H.; Brelid, H. Acid hydrolysis of cellulosic fibres: Comparison of bleached kraft pulp, dissolving pulps and cotton textile cellulose. Carbohydrate Polymers 2016, 136, 1281-1287.

67. Plasynski, S. I.; Chen, Z.-Y. Review of CO_2 capture technologies and some improvement opportunities. PDF file. Fall (Washington DC) 2000, 45(4), 644-911.

68. Preparation and Reactions of Carboxylic Acids. Learning Objectives 1-Synthesis (preparation) of carboxylic acids by: 1.1 Oxidation of primary alcohol. Retrieved from http://slideplayer.com/slide/7427733/

69. Quadrupole. (2016, June, 17). Retrieved from http://www.oxforddictionaries.com/definition/english/quadrupole

70. Radiative Forcing. (2011). Retrieved from http://www.co2offsetresearch.org/aviation/RF.html

71. Rockwood, D.N.; Preda, R.C.; Yucel, T.; Wang, X.; Lovett, M.L.; Kaplan, D.L. Materials fabrication from bombyx mori silk fibroin. Nat. Protocols 2011, 6, 1612-1631.

72. Sah, M. K.; Pramanik, K. Regenerated Silk Fibroin from B. mori Silk Cocoon for Tissue Engineering Applications. International Journal of Environmental Science and Development 2010, 1(5), 404-408.

73. Schell, W.J.; Wensley, C.G.; Chen, M.S.K.; Venugopal, K.G.; Miller, B.D.; Stuart, J.A. Recent advances in cellulosic membranes for gas separation and pervaporation. Gas Separation & Purification 1989, 3, 162-169.

74. Scholes, C.A.; Kentish, S.E.; Stevens, G.W. Carbon dioxide separation through polymeric membrane systems for flue gas applications. Recent Patents on Chemical Engineering 2008, 1, 52-66.

75. Shang, S.; Zhu, L.; Fan, J. Physical properties of silk fibroin/cellulose blend films regenerated from the hydrophilic ionic liquid. Carbohydrate Polymers 2011, 86, 462-468.

76. Shang, S.; Zhu, L.; Fan, J. Intermolecular interactions between natural polysaccharides and silk fibroin protein. Carbohydrate Polymers 2013, 93, 561-573.

77. Shieh, Y.-T.; Liu, K.-H. The effect of carbonyl group on sorption of CO_2 in glassy polymers. The Journal of Supercritical Fluids 2003, 25, 261-268.

78. Simons, K. Membrane technologies for CO_2 capture. Ph.D. Thesis. Faculty of Science and Technology, University of Twente. 2010.

79. Structure of cocoon silk. Retrieved from https://www.omicsonline.org/articles-images/2155-952X-S9-004-g005.html

80. Sun, C.; Lapudomlert, R.; Thepwatee, S. Power point file. “Coal Conversion and utilization for reducing CO_2 emissions from a power plant”.

81. Tan, C.-D.; Ni, J.F. Quantitative FTIR determination of extinction coefficients of adsorbed co. Journal of Chemical & Engineering Data 1997, 42, 342-345.

82. Tang, Q.-L.; Luo, Q.-H. Adsorption of CO_2 at ZnO: A surface structure effect from DFT+U calculations. The Journal of Physical Chemistry C 2013, 117, 22954-22966.

83. The Greenhouse Effect and Climate Change. (2014). Retrieved from http://www.penrithlakeseec.com/wp-content/uploads/2014/11/GreenhouseEffectAndClimateChange.pdf

84. The top Ten Green House Gases. (2009, March 17). Retrieved from http://www.popsci.com/environment/article/2009-03/top-ten-greenhouse-gases?image=8

85. Thiyam, P.; Persson, C.; Parsons, D.F.; Huang, D.; Buhmann, S.Y.; Boström, M. Trends of CO_2 adsorption on cellulose due to van der waals forces. Colloids and Surfaces A: Physicochemical and Engineering Aspects 2015, 470, 316-321.

86. Tsalagkas, D. Ph.D. Thesis. Bacterial cellulose thin-films for energy harvesting applications. Faculty of Engineering, Wood Sciences and Applied Arts, Univeristy of West Hungary. 2015.

87. Tudora, M.-R.; Zaharia, C.; Stancu, I.-C.; Vasile, E.; Truşcă, R.; Cincu, C. Natural silk fibroin micro- and nanoparticles with potential uses in drug delivery system. UPB Scientific Bulletin, Series B: Chemistry and Materials Science 2013, 75(1). 43-52.

88. Ulloa, C.J. Remediation of cellulose acetate gas separation membranes contaminated by heavy hydrocarbons. UWSpace, 2012.

89. Understanding Global Warming Potentials. (2016, August 9). Retrieved from https://www.epa.gov/ghgemissions/understanding-global-warming-potentials

90. Venturia, D.; Ansalonib, L.; Giacinti Baschetti, M. Nanocellulose Based Facilitated Transport Membranes for CO_2 Separation. Chemical Engineering Transactions 2016. 47, 349-354.

91. Wang, M.; Lawal, A.; Stephenson, P.; Sidders, J.; Ramshaw, C. Post-combustion CO_2 capture with chemical absorption: A state-of-the-art review. Chemical Engineering Research and Design 2011, 89, 1609-1624.

92. Wang, S.; Han, X. Application of Polymeric Membrane in CO_2 Capture from Post Combustion. Advances in Chemical Engineering and Science 2012, 2(3), 336-341.

93. Wang, S.; Huang, T.; Lai, C.; Xi, T.; Liao, S.; Nan, F. Oxidized nano-bacterial cellulose/silk fibroin composite films. Cellulose Chemistry and Technology 2016, 50(7-8), 853-862.

94. Wijmans, J.G.; Baker, R.W. The solution-diffusion model: A review. Journal of Membrane Science 1995, 107, 1-21.

95. What is Natural Gas? Retrieved from http://www.energy.alberta.ca/naturalgas/723.asp

96. Wu, J.; Yuan, Q. Gas permeability of a novel cellulose membrane. Journal of Membrane Science 2002, 204, 185-194.

97. Xing, R.; Ho, W.S.W. Synthesis and characterization of crosslinked polyvinylalcohol/polyethyleneglycol blend membranes for CO_2/CH_4 separation. Journal of the Taiwan Institute of Chemical Engineers 2009, 40, 654-662.

98. Xiong, G.; Pal, U.; Serrano, J.G.; Ucer, K.B.; Williams, R.T. Photoluminesence and FTIR study of ZnO nanoparticles: The impurity and defect perspective. physica status solidi (c) 2006, 3, 3577-3581.

99. Yamakawa, K.; Sato, Y.; Fukutani, K. Asymmetric and symmetric absorption peaks observed in infrared spectra of CO_2 adsorbed on TiO_2 nanotubes. The Journal of Chemical Physics 2016, 144, 154703.

100. Yang, G.; Zhang, L.; Liu, Y. Structure and microporous formation of cellulose/silk fibroin blend membranes: I. Effect of coagulants. Journal of Membrane Science 2000, 177, 153-161.

101. Yang, J.; Yan, X.; Xue, T.; Liu, Y. Enhanced CO_2 adsorption on al-mil-53 by introducing hydroxyl groups into the framework. RSC Advances 2016, 6, 55266-55271.

102. Yao, Y.; Nijem, N.; Li, J.; Chabal, Y.J.; Langreth, D.C.; Thonhauser, T. Analyzing the frequency shift of physiadsorbed CO_2 in metal organic framework materials. Physical Review. B. 2012, 064302.

103. Yeo, Z.Y.; Chew, T.L.; Zhu, P.W.; Mohamed, A.R.; Chai, S.-P. Conventional processes and membrane technology for carbon dioxide removal from natural gas: A review. Journal of Natural Gas Chemistry 2012, 21, 282-298.

104. Yu, C.-H.; Huang, C.-H.; Tan, C.-S. A Review of CO_2 Capture by Absorption and Adsorption. Aerosol and Air Quality Research 2012, 12, 745–769.

105. Yuan, Y.; Teja, A.S. Quantification of specific interactions between CO_2 and the carbonyl group in polymers via ATR-FTIR measurements. The Journal of Supercritical Fluids 2011, 56, 208-212.

106. Zhang, H.; Li, L.L.; Dai, F.Y., Zhang, H.H.; Ni, B.; Zhou, W.; Yang, X.; Wu, Y.Z. Preparation and characterization of silk fibroin as a biomaterial with potential for drug delivery. Journal of Translational Medicine 2012.

Appendix

Table 5. FTIR peak wavenumbers of cellulose, silk fibroin, and ZnO nanoparticles according to the literature (Fan et al., 2012; Zhang et al., 2012; Oliveira et al., 2015; Tsalagkas, 2015; Wang et al., 2016).

Peak wavenumbers (cm^{-1})	**Bonds**
3375-3340	Intra H-bond O(3)H---O(5)
3310-3230	Inter H-bond O(6)H--O(3)
2899	CH stretching
1660-1645	amide I (random coil conformation; silk I)
1655	α-helix conformation (silk I)
1640	OH bending of absorbed water
1630-1625	peptide backbone of amide I (C =O stretching) (β-sheet molecular conformation; silk II)
1550-1540	amide II (random coil conformation; silk I)
1530-1520	amide II (N-H bending) (β-sheet molecular conformation; silk II)
1600-1100	Zn-OH bending mode
1444	amide (III) (C-N stretching)
1426	CH_2 bending
1370	CH bending
1336	OH in plane bending
1314	CH_2 rocking vibration at C6
1280	O-H in-plane bending
1270-1265	amide (III) (C-N stretching) (β-sheet molecular conformation; silk II)
1230	amide III (random coil conformation; silk I)
1204	C-O-C symmetric stretching or OH in plane deformation
1158	C-O-C asymmetric stretching vibration
1108	nonsymmetric in-phase ring vibration

1055	C-O stretching
896	β-glucosidic linkages between the glucose units
400-700	OH bending, ZnO stretching modes

Table 6. IR peak wavenumbers of different carbonate species formed after interaction with CO_2 according to the literature (Galhotra and Grassian, 2010).

Peak wavenumbers (cm^{-1})	Vibrational mode
	Bicarbonate
1630 (1650-1610)	υ_2 (O-C-O)$_a$
1422 (1435-1424)	υ_3 (O-C-O)$_s$
1225 (1230-1228)	δ_4 (COH)
	Carbonate
	- Monodentate
1040-1030	υ_1 (C-O)$_s$
1375 (1404-1370)	υ_3 (O-C-O)$_s$
1475 (1480-1425)	υ_3 (O-C-O)$_a$
	- Bidentate
994 (1030-999)	υ_1 (C-O)$_s$
1334 (1364-1303)	υ_3 (O-C-O)$_s$
1608 (1665-1512)	υ_3 (O-C-O)$_a$
	Carboxylate
1030	υ_1 (C-O)$_s$
1288 (1382-1300)	υ_3 (O-C-O)$_s$
1522 (1580-1508)	υ_3 (O-C-O)$_a$